

JPL D-1000785

Surface Biology and Geology (SBG) Observing Terrestrial Thermal Emission Radiometer (OTTER)

Level 2 Land Surface Temperature and Emissivity Algorithm Theoretical Basis Document (ATBD)

Version 0.5
September 6, 2023

Glynn Hulley
Jet Propulsion Laboratory
California Institute of Technology

JPL D-1000785

© 2023 California Institute of Technology. Government sponsorship acknowledged.

Paper copies of this document may not be current and should not be relied on for official purposes. The current version is in the SBG DocuShare Library (*) at [insert url]
(* *Access limited to user group*)

National Aeronautics and
Space Administration



Jet Propulsion Laboratory
4800 Oak Grove Drive
Pasadena, California 91109-8099
California Institute of Technology

This research was carried out at the Jet Propulsion Laboratory, California Institute of Technology, under a contract with the National Aeronautics and Space Administration.

Reference herein to any specific commercial product, process, or service by trade name, trademark, manufacturer, or otherwise, does not constitute or imply its endorsement by the United States Government or the Jet Propulsion Laboratory, California Institute of Technology.

© 2023. California Institute of Technology. Government sponsorship acknowledged.

Change History Log

Revision	Effective Date	Authors	Description of Changes
V0.1	08/22/2023	Glynn Hulley	First draft
V0.5	09/06/2023	Glynn Hulley	Modification to section 5: Uncertainty analyses

Contacts

Readers seeking additional information about this study may contact the following:

Glynn C. Hulley (L2 Lead, Co-Investigator)

MS 183-501

Jet Propulsion Laboratory

4800 Oak Grove Dr.

Pasadena, CA 91109

Email: *glynn.hulley@jpl.nasa.gov*

Office: (818) 354-2979

Simon J. Hook (Principal Investigator)

MS 233-200

Jet Propulsion Laboratory

4800 Oak Grove Dr.

Pasadena, CA 91109

Email: *simon.j.hook@jpl.nasa.gov*

Office: (818) 354-0974

SBG Science Team

Team members:

Abstract

The 2017-2027 Decadal Survey for Earth Science and Applications from Space (ESAS 2017) was released in January 2018. ESAS 2017 was driven by input from the scientific community and policy experts and provides a vision and strategy for Earth observation that informs federal agencies responsible for the planning and execution of civilian space-based Earth-system programs in the coming decade, including the National Aeronautics and Space Administration (NASA), the National Oceanic and Atmospheric Administration (NOAA), and the U.S. Geological Survey (USGS). NASA has, thus far, utilized this document as a guide to inform exploration of new Earth mission concepts which are later considered as candidates for fully funded missions. High-priority emphasis areas and targeted observables include global-scale Earth science questions related to hydrology, ecosystems, weather, climate, and solid earth. One of the Designated Observables (DO's) identified by ESAS 2017 was Surface Biology and Geology (SBG) with a goal to acquire concurrent global hyperspectral visible to shortwave infrared (VSWIR; 380–2500 nm) and multispectral midwave and thermal infrared (MWIR: 3–5 μm ; TIR: 8–12 μm) imagery at high spatial resolution (~ 30 m in the VSWIR and ~ 60 m in the TIR) and sub-monthly temporal resolution globally. The final sensor characteristics will be determined during the mission formulation phase, but ESAS 2017 provides guidance for a VSWIR instrument with 30–45 m pixel resolution, ≤ 16 day global revisit, $\text{SNR} > 400$ in the VNIR, $\text{SNR} > 250$ in the SWIR, and 10 nm sampling in the range 380–2500 nm. It also recommends a TIR instrument with more than five channels in 8–12 μm , and at least one channel at 4 μm , ≤ 60 m pixel resolution, ≤ 3 day global revisit, and noise equivalent delta temperature (NEdT) ≤ 0.2 K (NASEM, 2018; Schimel et al., 2020). Alone, SBG will provide a comprehensive monitoring approach globally. Complemented with systems like Landsat and Sentinel-2, global change processes with faster than 16-day global change rates can be mapped—at lower spectral resolution—but high temporal revisit.

Contents

Contacts		i
SBG Science Team		ii
Abstract		iii
1 Introduction		1
2 SBG Instrument Characteristics		5
2.1 Band positions		5
2.2 Radiometer		7
3 Theory and Methodology		9
3.1 Midwave and Thermal Infrared Remote Sensing Background		9
3.2 Radiative Transfer Model		14
3.2.1 RTTOV		14
3.3 Atmospheric Profile Data		16
3.3.1 Profile Temporal Interpolation		20
3.3.2 Profile Vertical and Horizontal Interpolation		23
3.4 Radiative Transfer Sensitivity Analysis		24
3.5 Temperature and Emissivity Separation Approaches		26
3.5.1 Deterministic Approaches		27
3.5.2 Non-deterministic Approaches		29
4 Temperature Emissivity Separation (TES) Algorithm		32
4.1 Data Inputs		33
4.2 TES Limitations		34
4.3 TES Processing Flow		35
4.4 NEM Module		38
4.5 Removing Downwelling Sky Irradiance		38
4.6 Refinement of ϵ_{max}		39
4.7 Ratio Module		41
4.8 MMD Module		41
4.9 MMD vs. ϵ_{min} Regression		44
5 Uncertainty Analysis		46
5.6 Error Propagation		52
6 Emissivity anisotropy correction		58
6.1 MMD calibration curve with view angle dependence		59
7 Quality Control and Diagnostics		61
8 Scientific Data Set (SDS) Variables		65
9 Calibration/Validation Plans		67
9.1 Emissivity Validation Methodology		73
9.2 LST Validation Methodology		76
9.2.1 Radiance-based Approach		76
9.2.2 Temperature-based (T-based) LST Validation Method		81
Acknowledgements		84

10 **References** **85**

Figures

- Figure 1: SBG boxcar filters for two MIR bands and six TIR bands from 3.8-12.5 microns with a typical atmospheric transmittance spectrum in gray highlighting the atmospheric window regions. Note the spectral width and location of the filters are finalized (see Table 2), however the spectral shape will be determined when the detectors are fabricated.

 5
- Figure 2: Modeled SBG NEdT versus scene temperature for the two MIR and six TIR bands with time delay integration (TDI).

 9
- Figure 3: Simulated top-of-atmosphere radiance at sensor for solar (red) and infrared (blue) radiance components in the 3–13 μm region including the total atmospheric transmittance (black). The left image shows an example for desert sand (quartz) while right image is a simulation for a forest (redwood conifer) both at 300 K surface temperature and using a US standard atmosphere.

 13
- Figure 4: Simulated at sensor radiance components described in equation (1) in the MIR range (3-4.2 micron) for desert sand (left) and redwood conifer (right) for a surface at 300 K and US standard atmosphere. Note the large solar reflected component for desert sand, while for vegetation this component is negligible due to higher emissivity (low reflectance). For both surfaces, the downwelling thermal radiance and solar path radiances are the smallest components and account for less than 2% of total radiance.

 14
- Figure 5: Example profiles of Relative Humidity (RH) and Air Temperature from the NCEP GDAS product.

 17
- Figure 6: An example showing temporal interpolation of air temperature (left panels) and relative humidity (right panels) data from the NCEP GDAS product over Los Angeles, CA at different atmospheric levels from surface to the stratosphere. A linear and a constrained quadratic fit is used for data at 0, 6, 12, 18 UTC and 0 UTC on the following day. The results indicate that a quadratic fit is optimal for fitting air temperature data in the boundary layer and mid-troposphere, but that a linear fit is more representative at higher levels. This is also true for the relative humidity.

 22
- Figure 7: a) Illustration of interpolation in elevation. The black circles represent elevations at which the NWP profiles are defined. b) Illustration of spatial interpolation. The grid represents the layout of the pixels and the black circles the NWP points (not to scale). The radiative transfer parameters values at the four pertinent NWP points are interpolated to the location of the current pixel, represented by the gray circle.

 23
- Figure 8. Flow diagram showing all steps in the retrieval process in generating the SBG land surface temperature and emissivity product starting with thermal infrared (TIR) at-sensor radiances and progressing through atmospheric correction, cloud detection, and the temperature emissivity separation (TES) algorithm.

 36
- Figure 9. Flow diagram of the temperature emissivity separation (TES) algorithm in its entirety, including the NEM, RATIO and MMD modules. Details are included in the text, including information about the refinement of ϵ_{max} .

 37
- Figure 10. SBG simulated LST generated from a MASTER scene on 30 January 2018 over Mauna Loa and Kilauea volcanoes in Hawaii.

- 43
 Figure 11. SBG simulated emissivity for band TIR-3 (9 micron) from a MASTER scene on 30 January 2018 over Mauna Loa and Kilauea volcanoes in Hawaii.
- 44
 Figure 12. SBG calibration curve of minimum emissivity vs. min-max difference (MMD). The lab data (crosses) are computed from 150 spectra consisting of a broad range of terrestrial materials (rocks, sand, soil, water, vegetation, and ice).
- 45
 Figure 13. SBG calibration curve of minimum emissivity vs. min-max difference (MMD). The lab data (crosses) are computed from 150 spectra consisting of a broad range of terrestrial materials (rocks, sand, soil, water, vegetation, and ice).
- 47
 Figure 14. Locations of the 15,704 day and nighttime atmospheric soundings of temperature, moisture, and ozone of from the SeeBor V5.0 radiosounding database.
- 48
 Figure 15. Histograms displaying the LST accuracy results of a 6-band TES approach with SBG TIR band locations for standard atmosphere (left) and tropical atmosphere (right), and for three different error sources including model (TES retrieval), instrument noise (NEdT = 0.2 K) and atmospheric (10% relative humidity error, and 1 K temperature error). 10,000 Monte Carlo simulations were run using MODTRAN and input ECOLib spectra of rocks, sands, soils, and vegetation. The errorbar represents the standard deviation (precision) of the simulation run for all errors combined.
- Error! Bookmark not defined.**
- Figure 16. [INSERT LST uncertainty estimate from simulated MASTER data]
- 57
 Figure 17 (left) MMD curves as obtained by fitting equation 26 to directional emissivity data derived with the multi-sensor method, for seven of the VZA bins; (right) Coefficient a^3 of the MMD equation (eq. 26; blue) as function of the VZA and respective fitted curve (eq. 27; red).
- 61
 Figure 18. Difference between the MODIS (MOD11_L2) and ASTER (AST08) LST products and in-situ measurements at Lake Tahoe. The MODIS product is accurate to ± 0.2 K, while the ASTER product has a bias of 1 K due to residual atmospheric correction effects since the standard product does not use a Water Vapor Scaling (WVS) optimization model.
- 71
 Figure 19. Laboratory-measured emissivity spectra of sand samples collected at ten pseudo-invariant sand dune validation sites in the southwestern United States. The sites cover a wide range of emissivities in the TIR region.
- 74
 Figure 20. ASTER false-color visible images (top) and emissivity spectra comparisons between ASTER TES and lab results for Algodones Dunes, California; White Sands, New Mexico; and Great Sands, Colorado (bottom). Squares with blue dots indicate the sampling areas. ASTER error bars show temporal and spatial variation, whereas lab spectra show spatial variation.
- 75
 Figure 21. An example of the R-based validation method applied to the MODIS Aqua MOD11 and MOD21 LST products over six pseudo-invariant sand dune sites using all data during 2005. AIRS profiles and lab-

measured emissivities from samples collected at the sites were used for the R-based calculations.

.....
77

Figure 22. An example of the T-based validation results showing ECOSTRESS LST versus in situ LST measurements for all T-based sites at Lake Constance, Gobabeb, Lake Tahoe, Salton Sea and Russell ranch.

.....
83

Tables

Table 1: SBG measurement characteristics as compared to other spaceborne TIR instruments.

 3

Table 2: SBG final band positions and characteristics.

 6

Table 3: SBG TIR Instrument and Measurement Characteristics

 8

Table 4: Geophysical data available in the GEOS5-FP analyses product. Columns under Mandatory specify if the variables is needed for determining atmospheric correction parameters.

 19

Table 5: Percent changes in simulated SBG brightness temperatures for bands MIR-1 (4.0 μm) and TIR 1 (8.32 μm), 3 (9.07 μm), and 5 (10.3 μm) for changes in input geophysical parameters.

 25

Table 6. Simulated LST uncertainties using a 3-band and 5-band TES algorithm for 4 different surface classes with surface emissivity spectra from ECOLib (111 total samples), MODTRAN simulations, and 382 global radiosonde profiles. The LST uncertainty includes random errors in simulated air temperature (2 K), relative humidity profile (20%), and instrument noise (0.1 K) as discussed in the text.

 55

Table 7. Bit flags defined in the QC SDS for the 5-band ECOSTRESS algorithm.

 63

Table 8. The Scientific Data Sets (SDSs) for the ECOSTRESS L2 product.

 66

Table 9. ECOSTRESS targets include all of CONUS plus 1,000 km regions centered on climate hotspots, agricultural regions, and FLUXNET validation sites. ENF: evergreen needleleaf forest; EBF: evergreen broadleaf forest; WSA: woody savanna; SAV: Savanna; CRO: cropland; DBF: Deciduous Broadleaf Forest; Cal/Val: LST Calibration/Validation.

 69

Table 10. Uncertainty analysis results showing how perturbations in emissivity, air temperature and relative humidity affect the relative accuracy of the R-based LST derivation.

 80

Table 11. R-based LST validation statistics from six pseudo-invariant sand dune sites using all MOD11 and MOD21 LST retrievals during 2005.

 80

Table 12. Emissivity comparisons between lab, MOD11, and MOD21 at six pseudo-invariant sand sites.

 81

1 Introduction

The Surface Biology and Geology (SBG) thermal infrared (TIR) instrument – termed the Observing Thermal Emission Radiometer (OTTER) consists of a TIR multispectral scanner with six spectral bands operating between 8 and 12.5 μm and two mid-infrared (MIR) bands at 4 μm and 4.8 μm , with a 60 m pixel resolution, 3 day global revisit, and noise equivalent delta temperature (NE Δ T) ≤ 0.2 K (NASEM, 2018; Schimel et al., 2020). The TIR data will be acquired at a spatial resolution of 60m x 60m with a swath width of 935 km (60°) from an altitude of ~ 700 km. This document outlines the theory and methodology for generating the OTTER Level-2 (L2) land surface temperature and emissivity (LST&E) products. The LST product is derived from the six TIR spectral bands between 8 and 12.5 μm , while the emissivity is retrieved for all 6 TIR and 2 MIR bands. The LST&E products are retrieved from the surface spectral radiance that is obtained by atmospherically correcting the at-sensor spectral radiance. Knowledge of the surface emissivity is critical for accurately recovering the surface temperature, a key climate variable in many scientific studies from climatology to hydrology, modeling the greenhouse effect, drought monitoring, and land surface models (Anderson et al. 2007; French et al. 2005; Jin and Dickinson 2010).

In addition to surface energy balance, LST&E products are essential for a wide range of other Earth system studies. For example, emissivity spectral signatures are important for geologic studies and mineral mapping studies (Hook et al. 2005; Vaughan et al. 2005). This is because emissivity features in the TIR region are unique for many different types of materials that make up the Earth's surface, for example, quartz, which is ubiquitous in most of the arid regions of the world. Emissivities are also used for land use and land cover change mapping since vegetation fractions can often be inferred if the background soil is observable (French et al. 2008).

The SBG TIR measurement derives its heritage from the ECOSTRESS measurement in terms of number of bands and spatial resolution. ECOSTRESS is a five-channel multispectral TIR scanner that was launched to the International Space Station (ISS) in June 2018 and has a 70-m spatial resolution and revisit time that is variable between 3-5 days on average. The OTTER L2 LST product will be validated with a combination of Temperature-based (Coll et al. 2005; Hook et al. 2004) and Radiance-based methods (Hulley and Hook 2012; Wan and Li 2008) using a global set of validation sites. The L2 emissivity product will be validated using a combination of lab-measured samples collected at various sand dune sites, and with the ASTER Global Emissivity Database (ASTER GED) (Hulley and Hook 2009b).

Maximum radiometric emission for the typical range of Earth surface temperatures, excluding fires and volcanoes, is found in two infrared spectral "window" regions: the midwave infrared (3.5–5 μm) and the thermal infrared (8–13 μm). The radiation emitted in these windows for a given wavelength is a function of both temperature and emissivity. Determining the separate contribution from each component in a radiometric measurement is an ill-posed problem since there will always be more unknowns— N emissivities and a single temperature—than the number of measurements, N , available. For SBG, we will be solving for one temperature and eight emissivities. Therefore, an additional constraint is needed, independent of the data. There have been numerous theories and approaches over the past two decades to solve for this extra degree of freedom. For example, the ASTER Temperature Emissivity Working Group (TEWG) analyzed ten different algorithms for solving the problem (Gillespie et al. 1999). Most of these relied on a radiative transfer model to correct at-sensor radiance to surface radiance and an emissivity model to separate temperature and

Table 1: SBG measurement characteristics as compared to other spaceborne TIR instruments.

Instrument	Platform	Resolution (m)	Revisit (days)	Daytime overpass	TIR bands (8-12.5 μm)	Launch year
OTTER	SBG	60	3	12:30 pm	6	2028*
ECOSTRESS	ISS	38 \times 68	3-5	Multiple	5	2018
ASTER	Terra	90	16	10:30 am	5	1999
ETM+/TIRS	Landsat 7/8	60-100	16	10:11 am	1/2	1999/2013
VIIRS	Suomi-NPP	750	Daily	1:30 am/pm	4	2011
MODIS	Terra/Aqua	1000	Daily	10:30/1:30 am/pm	3	1999/2002
GOES	Multiple	4000	Daily	Every 15 min	2	2000

emissivity. Other approaches include the split-window (SW) algorithm, which extends the SST SW approach to land surfaces, assuming that land emissivities in the window region (10.5–12 μm) are stable and well known. However, this assumption leads to unreasonably large errors over barren regions where emissivities have large variations both spatially and spectrally. The ASTER TEWG finally decided on a hybrid algorithm, termed the temperature emissivity separation (TES) algorithm, which capitalizes on the strengths of previous algorithms with additional features (Gillespie et al. 1998).

TES is applied to the land-leaving TIR radiances that are estimated by atmospherically correcting the at-sensor radiance on a pixel-by-pixel basis using a radiative transfer model. TES uses an empirical relationship to predict the minimum emissivity that would be observed from a given spectral contrast, or minimum-maximum difference (MMD) (Kealy and Hook 1993; Matsunaga 1994). The empirical relationship is referred to as the calibration curve and is derived from a subset of spectra in the ASTER spectral library (Baldrige et al. 2009). A new calibration

curve, applicable to SBG TIR bands, will be computed using the latest ECOSTRESS spectral library v2 (Meerdink et al. 2019), in addition to spectra from 9 pseudo-invariant sand dune sites located in the US Southwest (Hulley et al. 2009a). TES has been shown to accurately recover temperatures within 1 K and emissivities within 0.015 for a wide range of surfaces and is a well established physical algorithm that produces seamless images with no artificial discontinuities such as might be seen in a land classification type algorithm (Gillespie et al. 1998).

The remainder of the document will discuss the SBG instrument characteristics, provide a background on TIR remote sensing, give a full description and background on the atmospheric correction and the TES algorithm, provide quality assessment, discuss numerical simulation studies and, finally, outline a validation plan.

2 SBG Instrument Characteristics

2.1 Band positions

The TIR instrument will acquire data from a sun-synchronous orbit of 700 km with 60m spatial resolution in eight spectral bands located in the MIR (2) and TIR (6) part of the electromagnetic spectrum between 4 and 12.5 μm shown in Figure 1. The center position and width of each band is provided in Table 2. The positions of three of the TIR bands closely match the first three thermal bands of ASTER, while two of the TIR bands match bands of ASTER and MODIS typically used for split-window type applications (ASTER bands 12–14 and MODIS bands 31, 32). It is expected that small adjustments to the band positions will be made based on ongoing engineering filter performance capabilities.

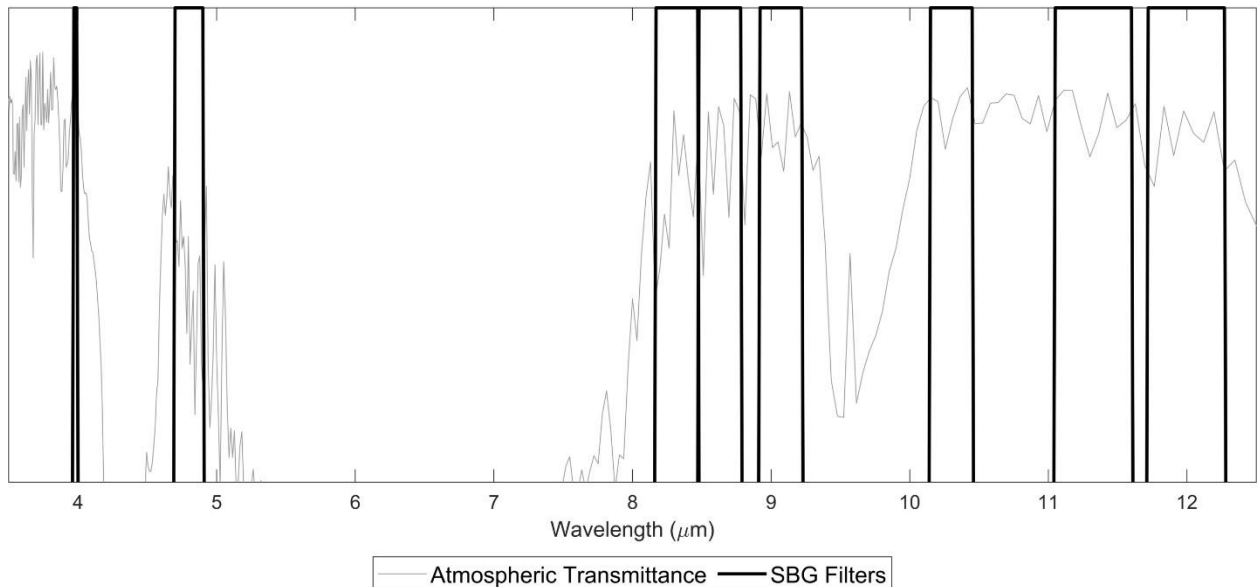


Figure 1: SBG boxcar filters for two MIR bands and six TIR bands from 3.8-12.5 microns with a typical atmospheric transmittance spectrum in gray highlighting the atmospheric window regions. Note the spectral width and location of the filters are finalized (see Table 2), however the spectral shape will be determined when the detectors are fabricated.

Table 2: SBG final band positions and characteristics.

Band #	Center Wavelength (μm)	Spectral Width (FWHM) (nm)	Tolerance Center Wavelength (\pm nm)	Tolerance Spectral Width (\pmnm)	Knowledge Center Wavelength (\pmnm)	Knowledge Spectral Width (\pmnm)	Accuracy (Kelvin)	NEdT (Kelvin)	Range (Kelvin)
MIR-1	3.98	20 (TBC)	50	10	10	10	$\leq 3@750$	$\leq 0.3@750$	700-1200
MIR-2	4.8	150 (TBC)	100	50	20	20	$\leq 1@450$	$\leq 0.2@450$	400-800
TIR-1	8.32	300 (TBC)	100	50	20	20	$\leq 0.5@275$	$\leq 0.2@275$	200-500
TIR-2	8.63	300 (TBC)	100	50	20	20	$\leq 0.5@275$	$\leq 0.2@275$	200-500
TIR-3	9.07	300 (TBC)	100	50	20	20	$\leq 0.5@275$	$\leq 0.2@275$	200-500
TIR-4	10.30	300 (TBC)	50	50	20	20	$\leq 0.5@275$	$\leq 0.2@275$	200-500
TIR-5	11.35	500 (TBC)	100	50	20	20	$\leq 0.5@275$	$\leq 0.2@275$	200-500
TIR-6	12.05	500 (TBC)	100	50	20	20	$\leq 0.5@275$	$\leq 0.2@275$	200-500

The TIR instrument will operate as a push-whisk mapper very similar to ECOSTRESS with 256 pixels in the cross-whisk direction for each spectral channel (Figure 2), which enables a wide swath and high spatial resolution. As the spacecraft moves forward, the scan mirror sweeps the focal plane ground projection in the cross-track direction. Each sweep is 256-pixels wide. The different spectral bands are swept across a given point on the ground sequentially. From the spacecraft altitude of 665 km, the resulting swath is 935 km wide. The scan mirror rotates at a constant angular speed and sweeps the focal plane image 68.8° across nadir, then to two on-board blackbody targets at 300 K and 340 K. Both blackbodies will be viewed with each cross-track sweep every 1.29 seconds to provide gain and offset calibrations.

2.2 Radiometer

[Updated info here on radiometer]

Table 3: SBG TIR Instrument and Measurement Characteristics

Spectral	
Bands (µm)	4, 4.8, 8.32, 8.63, 9.07, 10.3, 11.35, 12.05
Bandwidth (nm)	20, 150, 300, 300, 300, 300, 500, 500
Accuracy at 300 K	<0.01 µm
Radiometric	
Range	TIR bands (200 - 500 K) 4 micron band (700 -1200 K) 4.8 micron band (400 - 800 K)
Resolution	< 0.05 K, linear quantization to 14 bits
Accuracy	< 0.5 K 3-sigma at 275 K
Precision (NEdT)	< 0.2 K
Linearity	>99% characterized to 0.1 %
Spatial	
IFOV	60m
MTF	>0.65 at FNy
Scan Type	Push-Whisk
Swath Width at 665-km altitude	935 km (+/- 34.4°)
Cross Track Samples	10,000 (check)
Swath Length	
Down Track Samples	256
Band to Band Co-Registration	0.2 pixels (12 m)
Pointing Knowledge	10 arcsec (0.5 pixels) (approximate value, currently under evaluation)
Temporal	
Orbit Crossing	Multiple
Global Land Repeat	Multiple
On Orbit Calibration	
Lunar views	1 per month {radiometric}
Blackbody views	1 per scan {radiometric}
Deep Space views	1 per scan {radiometric}
Surface Cal Experiments	2 (day/night) every 5 days {radiometric}
Spectral Surface Cal Experiments	1 per year
Data Collection	
Time Coverage	Day and Night
Land Coverage	Land surface above sea level
Water Coverage	n/a
Open Ocean	n/a
Compression	2:1 lossless

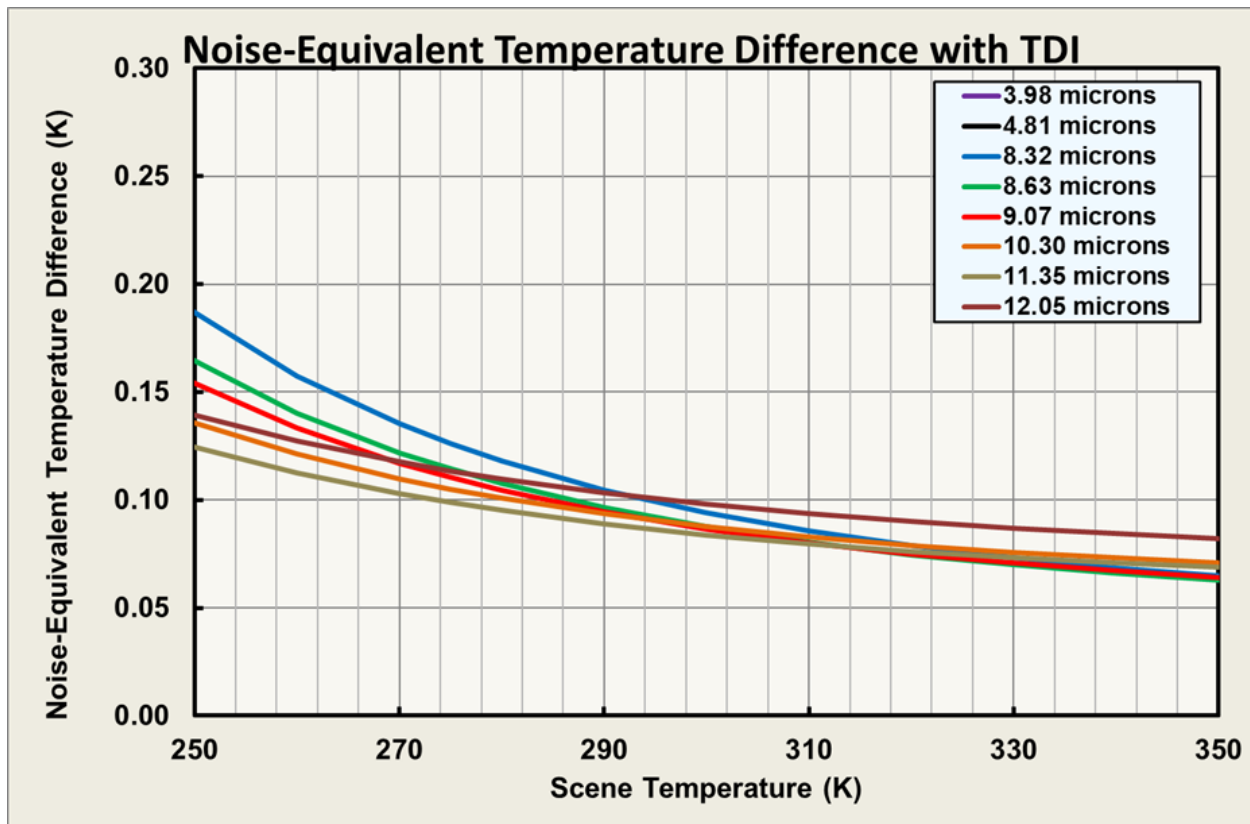


Figure 2: Modeled SBG NEdT versus scene temperature for the two MIR and six TIR bands with time delay integration (TDI).

3 Theory and Methodology

3.1 Midwave and Thermal Infrared Remote Sensing Background

The at-sensor measured radiance in the infrared region (4–15 μm , MIR: 3–5 μm , TIR: 8–15 μm) consists of a combination of different terms from surface emission, solar reflection, and atmospheric emission and attenuation. The Earth-emitted radiance is a function of temperature and emissivity and gets attenuated by the atmosphere on its path to the satellite. The emissivity of an isothermal, homogeneous emitter is defined as the ratio of the actual emitted radiance to the radiance emitted from a black body at the same thermodynamic temperature (Norman and Becker

1995), $\epsilon_\lambda = R_\lambda / B_\lambda$. The emissivity is an intrinsic property of the Earth's surface and is an independent measurement of the surface temperature, which varies with irradiance and local atmospheric conditions. The emissivity of most natural Earth surfaces for the TIR wavelength ranges between 8 and 12 μm and, for a sensor with spatial scales <100 m, varies from ~ 0.7 to close to 1.0. Narrowband emissivities less than 0.85 are typical for most desert and semi-arid areas due to the strong quartz absorption feature (reststrahlen band) between the 8- and 9.5- μm range, whereas the emissivity of vegetation, water, and ice cover are generally greater than 0.95 and spectrally flat in the 3–15- μm range except for dry and senesced vegetation that can have emissivities range from 0.9-0.95 in the longer wavelengths above 10 μm .

The atmosphere also emits radiation, of which some reaches the sensor directly as "path radiance," while some gets radiated to the surface (irradiance) and reflected back to the sensor, commonly known as the reflected downwelling sky irradiance. One effect of the sky irradiance is the reduction of the spectral contrast of the emitted radiance, due to Kirchhoff's law. Assuming the spectral variation in emissivity is small (Lambertian assumption), and using Kirchhoff's law to express the hemispherical-directional reflectance as directional emissivity ($\rho_\lambda = 1 - \epsilon_\lambda$), The at-sensor measured radiance in the infrared spectral region (3–15 μm) is a combination of three primary terms: the Earth-emitted radiance, reflected downwelling radiance (thermal + solar components), and total atmospheric path radiance (thermal + solar components).

$$L_{obs}(\lambda, \theta) = \tau_\lambda(\theta) \left[\epsilon_\lambda B(\lambda, T_s) + \rho_\lambda \left(L_s^\downarrow(\lambda, \theta) + L_t^\downarrow(\lambda, \theta) \right) \right] + L_t^\uparrow(\lambda, \theta) + L_s^\uparrow(\lambda, \theta) \quad (1)$$

where: $L(\lambda, \theta)$ = at-sensor radiance, λ is wavelength, θ is the satellite viewing angle, ϵ_λ is the surface emissivity, ρ_λ is surface reflectance, $B(\lambda, T_s)$ is the Planck function describing radiance emitted at surface temperature, T_s , L_s^\downarrow is the total (diffuse and direct) downwelling solar radiance,

L_t^\downarrow is the downwelling thermal irradiance, $\tau_\lambda(\theta)$ is the atmospheric transmittance, $L_s^\uparrow(\lambda, \theta)$ is the upward path solar radiance, and $L_t^\uparrow(\lambda, \theta)$ is the upward thermal path radiance reaching the sensor.

Reflected solar radiation in the midwave infrared (MIR, 3-5 μm) region is non-negligible for highly reflective surfaces and needs to be taken into account in the atmospheric correction. For example, Figure 3 shows that the solar contribution to at-sensor radiance is almost the same magnitude as the thermal component between 3-4 μm for highly reflective quartz sands ($\sim 1 \text{ W/m}^2$), while the solar component is negligible for a simulated vegetative surface (e.g. conifer). Typically the diffuse and direct solar beam terms are estimated and treated separately since the solar zenith angle has different effects on these terms. For example, with high solar zenith angles the solar beam at the surface decreases, but the solar diffuse irradiance term may increase. For most terrestrial surfaces the emissivity varies between 0.6 and 1 in the MIR, but values less than 0.85 are mostly restricted to deserts. Even though there are significant spectral variations in this region, their BRDF anisotropic factor is small and on the order of 2%. As a result we can assume a single BRDF factor and Lambertian surface with isotropic reflection i.e. $\rho_\lambda = \frac{\rho_\lambda}{\pi}$.

The reflected thermal infrared (TIR, 8-15 μm) radiance term is generally smaller in magnitude ($\sim 10\%$) than the surface-emitted radiance but needs to be taken into account particularly over highly reflective surfaces and on humid days when atmospheric water vapor content is high. Because of the smaller sky irradiance contribution and generally low reflectances in the TIR region over most vegetated surfaces, we can also assume a Lambertian surface and use Kirchhoff's law to express the hemispherical-directional reflectance as directional emissivity i.e. $\rho_\lambda = \frac{1-\epsilon_\lambda}{\pi}$. Equation (1) gives the at-sensor radiance for a single wavelength, λ , while the measurement from a sensor is typically measured over a range of wavelengths, or band. The at-sensor radiance for a discrete band, i , is obtained by weighting and normalizing the at-sensor spectral radiance

calculated by equation (1) with the sensor's spectral response function for each band, Sr_λ , as follows:

$$L_i(\theta) = \frac{\int Sr_\lambda(i) \cdot L_\lambda(\theta) \cdot d\lambda}{Sr_\lambda(i) \cdot d\lambda} \quad (2)$$

Based on these assumptions we can express the total at-sensor radiance measured by a sensor for band i as:

$$L_i(\theta) = \tau_i(\theta) \left[\epsilon_i B(i, T_s) + \frac{1-\epsilon_i}{\pi} (L_s^\downarrow(i, \theta) + L_t^\downarrow(i, \theta)) \right] + L_t^\uparrow(i, \theta) + L_s^\uparrow(i, \theta) \quad (3)$$

The atmospheric and solar terms (L_s^\downarrow , L_t^\downarrow , τ_λ , L_s^\uparrow , L_t^\uparrow) can be estimated with a suitable radiative transfer model such as MODTRAN (Berk et al. 2005; Kneizys et al. 1996) or RTTOV, using input atmospheric fields of air temperature, relative humidity, and geopotential height from either remote sounding data (e.g. IASI, AIRS), or from Numerical Weather Model (NWP) data (e.g. ECMWF, MERRA2, NCEP). For the atmospheric correction of MODIS and VIIRS Infrared data, both temperature/emissivity separation algorithms used to produce the LST&E products (MOD21, VNP21) use the [RTTOV](#) model, which was found to be an order of magnitude faster in compute time than MODTRAN. The RTTOV model was developed by the European Center for Medium range Weather Forecasting (ECMWF) (Matricardi et al. 2004) and uses FORTRAN 90 code with a spectral range in the visible/infrared from 0.4 – 50 μm . More detailed information on RTTOV is available in Matricardi (2004) and Bauer (2006).

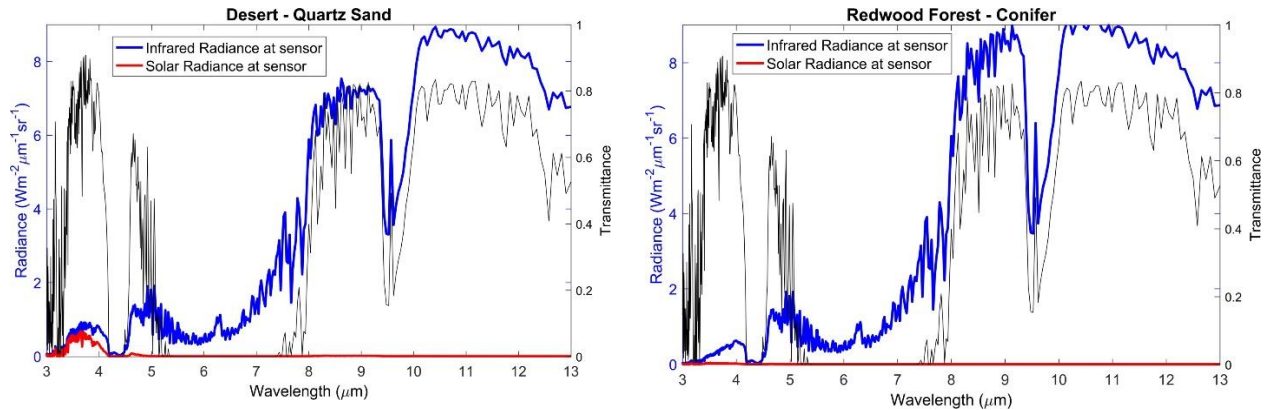


Figure 3: Simulated top-of-atmosphere radiance at sensor for solar (red) and infrared (blue) radiance components in the 3–13 μm region including the total atmospheric transmittance (black). The left image shows an example for desert sand (quartz) while right image is a simulation for a forest (redwood conifer) both at 300 K surface temperature and using a US standard atmosphere.

To further speed up computational time a Look Up Table (LUT) approach can be implemented to estimate the solar components (L_S^\downarrow , L_S^\uparrow) based on input day of year, satellite zenith angle, and solar zenith angle. For the MOD21 and VNP21 TES algorithms, these LUT’s were calculated using MODTRAN runs with a step for satellite and solar zenith angles of 10 degrees for angles smaller than 30, and 5 degrees for angles larger, and up to 65 degrees for satellite and 75 for solar angles. A step of one day per month for a year was used for the day of year constraint (i.e. solar constant changes).

The approach for computing surface radiance is essentially a two-step process. First, the atmospheric state is characterized by obtaining atmospheric profiles of air temperature, water vapor, geopotential height, and ozone at the observation time and location of the measurement. Ideally the profiles should be obtained from a validated, mature product with sufficient spatial resolution and close enough in time with the ECOSTRESS observation to avoid interpolation errors. This is particularly important for the temperature and water profiles to ensure good accuracy. Absorption from other gas species such as CH_4 , CO , and N_2O will not be significant

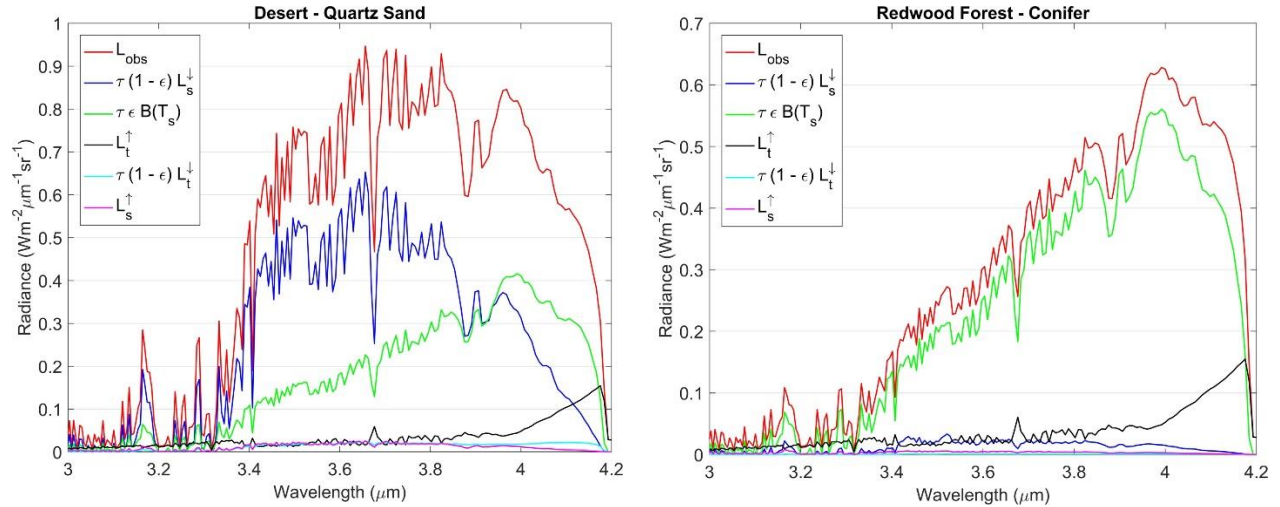


Figure 4: Simulated at sensor radiance components described in equation (1) in the MIR range (3-4.2 micron) for desert sand (left) and redwood conifer (right) for a surface at 300 K and US standard atmosphere. Note the large solar reflected component for desert sand, while for vegetation this component is negligible due to higher emissivity (low reflectance). For both surfaces, the downwelling thermal radiance and solar path radiances are the smallest components and account for less than 2% of total radiance.

for the placement of the ECOSTRESS TIR bands. The second step is to input the atmospheric profiles to a radiative transfer model to estimate the atmospheric parameters defined previously. This method will be used on clear-sky pixels only, which will be classified using a cloud mask specifically tailored for ECOSTRESS data. Clouds result in strong attenuation of the thermal infrared signal reaching the sensor, and an attempt to correct for this attenuation will not be made.

3.2 Radiative Transfer Model

3.2.1 RTTOV

The Radiative Transfer for TOVS ([RTTOV](#)) is a very fast radiative transfer model for nadir-viewing passive visible, infrared and microwave satellite radiometers, spectrometers and interferometers (Saunders et al. 1999). RTTOV is a FORTRAN-90 code for simulating satellite radiances, designed to be incorporated within users' applications. RTTOV was originally developed at ECMWF in the early 90's for TOVS (Eyre and Woolf 1988). Subsequently the

original code has gone through several developments (Matricardi et al. 2001; Saunders et al. 1999), more recently within the EUMETSAT NWP Satellite Application Facility (SAF), of which RTTOV v11 is the latest version. It is actively developed by ECMWF and UKMET.

A number of satellite sensors are supported from various platforms (https://nwpsaf.eu/deliverables/rtm/rttov_description.html). RTTOV has been sufficiently tested and validated and is conveniently fast for full scale retrievals (Matricardi 2009). Given an atmospheric profile of temperature, water vapor and optionally other trace gases (for example ozone and carbon dioxide) together with satellite and solar zenith angles and surface temperature, pressure and optionally surface emissivity and reflectance, RTTOV will compute the top of atmosphere radiances in each of the channels of the sensor being simulated. Users can also specify the selected channels to be simulated.

Mathematically, in vector notation, given a state vector, \mathbf{x} , which describes the atmospheric/surface state as a profile and surface variables the radiance vector, \mathbf{y} , for all the channels required to be simulated is given by (Saunders et al. 1999):

$$\mathbf{y} = H(\mathbf{x}) \tag{4}$$

where H is the radiative transfer model, i.e. RTTOV (also referred to as the observation operator in data assimilation parlance). This is known as the 'direct' or 'forward' model.

An important feature of the RTTOV model is that it not only performs the fast computation of the forward (or direct) clear-sky radiances but also the fast computation of the gradient of the radiances with respect to the state vector variables for the input state vector values. The Jacobian matrix \mathbf{H} which gives the change in radiance $\delta\mathbf{y}$ for a change in any element of the state vector $\delta\mathbf{x}$ assuming a linear relationship about a given atmospheric state \mathbf{x}_0 :

$$\delta\mathbf{y} = \mathbf{H}(\mathbf{x}_0)\delta\mathbf{x} \tag{5}$$

The elements of \mathbf{H} contain the partial derivatives $\frac{\partial y_i}{\partial x_j} \left(\frac{dy_i}{dx_j} \right)$ where the subscript i refers to channel number and j to position in state vector. The Jacobian gives the top of atmosphere radiance change for each channel from each level in the profile given a unit perturbation at any level of the profile vectors or in any of the surface/cloud parameters. It shows clearly, for a given profile, which levels in the atmosphere are most sensitive to changes in temperature and variable gas concentrations for each channel.

In RTTOV the transmittances of the atmospheric gases are expressed as a function of profile dependent predictors. This parameterization of the transmittances makes the model computationally efficient. The RTTOV fast transmittance scheme uses regression coefficients derived from accurate Line by Line computations to express the optical depths as a linear combination of profile dependent predictors that are functions of temperature, absorber amount, pressure and viewing angle (Matricardi and Saunders 1999). The regression coefficients are computed using a training set of diverse atmospheric profiles chosen to represent the range of variations in temperature and absorber amount found in the atmosphere (Chevallier 2000; Matricardi 2008, 2009; Matricardi and Saunders 1999). The selection of the predictors is made according to the coefficients file supplied to the program.

3.3 Atmospheric Profile Data

The general methodology for atmospherically correcting TIR data is based on the methods that were developed for the ASTER (Palluconi et al. 1999) and MODIS approaches (Hulley et al. 2012a). However, adjustments will be made by taking advantage of improved interpolation techniques and higher resolution Numerical Weather Prediction (NWP) model data.

Currently two options for atmospheric profile sources are available: 1) interpolation of data assimilated from NWP models, and 2) retrieved atmospheric geophysical profiles from remote-sensing data. The NWP models use current weather conditions, observed from various sources (e.g., radiosondes, surface observations, and weather satellites) as input to dynamic mathematical models of the atmosphere to predict the weather. Data are typically output in 6-hour increments, e.g., 00, 06, 12, and 18 UTC. Examples include the Global Data Assimilation System (GDAS) product provided by the National Centers for Environmental Prediction (NCEP)

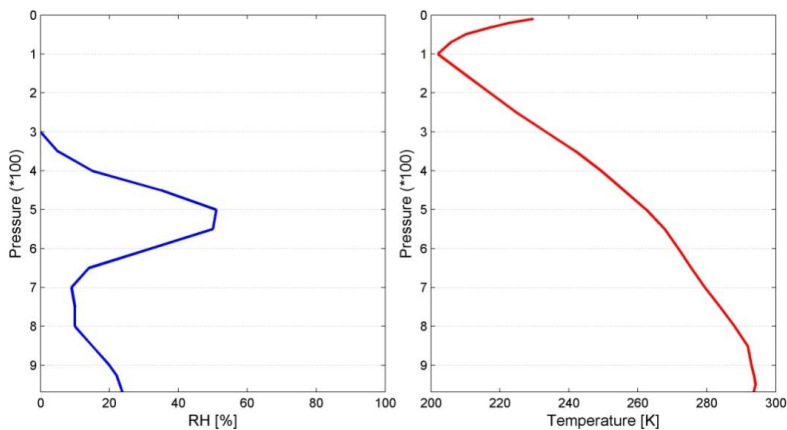


Figure 5: Example profiles of Relative Humidity (RH) and Air Temperature from the NCEP GDAS product.

(Kalnay et al. 1990), the Modern Era Retrospective-analysis for Research and Applications (MERRA-2) product provided by the Goddard Earth Observing System Data Assimilation System Version 5.2.0 (GEOS-5.2.0) (Bosilovich et al. 2008), GEOS-5 Forward Processing (FP) Atmospheric Data Assimilation System (GEOS-5 ADAS), and the European Center for Medium-Range Weather Forecasting (ECMWF), which is supported by more than 32 European states. Remote-sensing data, on the other hand, are available real-time, typically twice-daily and for clear-sky conditions. The principles of inverse theory are used to estimate a geophysical state (e.g., atmospheric temperature) by measuring the spectral emission and absorption of some known chemical species such as carbon dioxide in the thermal infrared region of the

electromagnetic spectrum (i.e. the observation). Examples of current remote sensing data include the Atmospheric Infrared Sounder (AIRS) (Susskind et al. 2003) and Moderate Resolution Imaging Spectroradiometer (MODIS) (Justice and Townshend 2002), both on NASA's Aqua satellite launched in 2002.

SBG will have a unique 12:30 am/pm overpass that does not overlap with current and likely future sounders (e.g. AIRS, CrIS, IASI) that usually have early afternoon overpass time (1:30 am/pm) and so the only feasible way to atmospherically correct the data at a given observation hour is to interpolate in space and time from NWP data. NWP data options available for SBG include the MERRA-2 and GEOS5 reanalyses products produced by the NASA Global Modeling and Assimilation Office (GMAO) and NOAA provided NWP data, e.g. NFS and NCEP. The likely choice for SBG will be the GEOS5-FP data that will provide consistency from ECOSTRESS. GEOS5-FP data provide the highest spatial (1/4 degree) and temporal (3 hourly) resolution and is provided in near real-time for end users. MERRA-2 data has a one month latency which would have complicated the processing system dynamics at the JPL science data system. The GEOS-5 FP Atmospheric Data Assimilation System (GEOS-5 ADAS) uses an analysis developed jointly with NOAA's National Centers for Environmental Prediction (NCEP), which allows the Global Modeling and Assimilation Office (GMAO) to take advantage of the developments at NCEP and the Joint Center for Satellite Data Assimilation (JCSDA) (Lucchesi 2017).

The atmospheric profiles are first interpolated in time to the SBG observation using the [00 03 06 09 12 15 18 21] analysis observation hours using a constrained quadratic function as discussed in the following section. The GEOS5 data is then gridded to the SBG swath resolution using a bicubic interpolation approach. The SRTM Digital Elevation Model (DEM) available in

Table 4: Geophysical data available in the GEOS5-FP analyses product. Columns under Mandatory specify if the variables is needed for determining atmospheric correction parameters.

GEOS5-FP Analyses Data (inst3_3d_asm_Np)				
Geophysical fields		Mandatory for RTTOV?	Available in GEOS5?	Remarks
time	Time	Yes	Yes	
lat	Latitude	Yes	Yes	
lon	Longitude	Yes	Yes	
lev	Pressure	Yes	Yes	
T	Air Temperature	Yes	Yes	
QV	Specific Humidity	Yes	Yes	Specific humidity is converted into ppmv for input to RTTOV
PS	Surface Pressure	Yes	Yes	
skt	Skin Temperature	Yes	No	T value at the first valid level above surface is used
t2	Temperature at 2 m	Yes	No	T value at the first valid level above surface is used
q2	Specific Humidity at 2 m	Yes	No	Q value at the first valid level above surface is used
lsm	Land Sea Mask	Yes	No	Auxiliary database SBG L1A GEO Data
el	Elevation	Yes	No	Auxiliary database SBG L1A GEO Data
tcw	Total Column Water	No	No	But calculated internally from QV levels, and used for L2 uncertainty estimation.
Resolution				
Frequency: 3 hr analysis from 00:00 UTC				
Spatial: 3D Grid, 1/4 degree in latitude × 5/16 degree in longitude				
Dimensions: 1152 (longitude) x 721 (latitude), 42 pressure levels				
Granule size: 558 MB				

the L1B product will be used to crop the profiles at the appropriate levels for each SBG pixel at native resolution.

3.3.1 Profile Temporal Interpolation

The diurnal cycle of near surface air temperature oscillates almost sinusoidally between a minimum at sunrise and a maximum in the afternoon. This occurs primarily because the atmosphere is relatively transparent to the shortwave radiation from the sun and relatively opaque to the thermal radiation from the Earth and as a result the surface is warmed by a positive daytime net radiation, and cooled by a negative nighttime radiation balance (radiative cooling). The net radiation determines whether the temperature rises, falls, or remains constant. The peak in daily temperature generally occurs in the afternoon as the air continues to warm due to a positive net radiation that persists for a few hours after noon (temperature lag). Similarly, minimum daily temperatures generally occur substantially after midnight, and sometimes during early morning hours around dawn, since heat is lost all night long. This effect can be seen in Figure 5 which shows air temperature (left panels) and relative humidity (right panels) data from the NCEP GDAS product over Los Angeles, CA for the 0, 6, 12, 18 UTC and 0 UTC on the following day. The air temperature diurnal cycle near the surface (1000 mb) shows a maximum temperature around 5 pm local time (12 pm UTC) during the summertime (1 August 2004), and a minimum at 4 am local (12 am UTC). A quadratic fit (red line) to the 5 data points captures the sinusoidal diurnal pattern quite well with maximum difference of ~ 1 K from the linear fit (black line). The maximum diurnal variation at 1000 mb for this particular day was ~ 7 K, decreasing to ~ 1 K above the boundary layer (850 mb), and on the order of a few degrees in the troposphere (250 mb). This indicates that a linear fit might be good enough above the boundary layer.

This is particularly evident for the relative humidity (RH) diurnal cycle, where large differences can be seen between the linear and quadratic fits at 250 mb due to a double inflection point. RH is the amount of moisture in the air compared to what the air can "hold" at that temperature and is generally calculated in relation to saturated water vapor density. When the air can't "hold" all the moisture, then it condenses as dew. Because of this the diurnal variation in RH is approximately inverse to that of temperature. At about sunrise the RH is typically at a maximum and reaches a minimum in the afternoon hours. The annual variation of RH is largely depends upon the locality. At regions where the rainy season is in summer and winter is dry, the maximum RH occurs in summer and minimum in winter and at other regions maximum RH occurs in winter. Over oceans the RH reaches a maximum during the summertime.

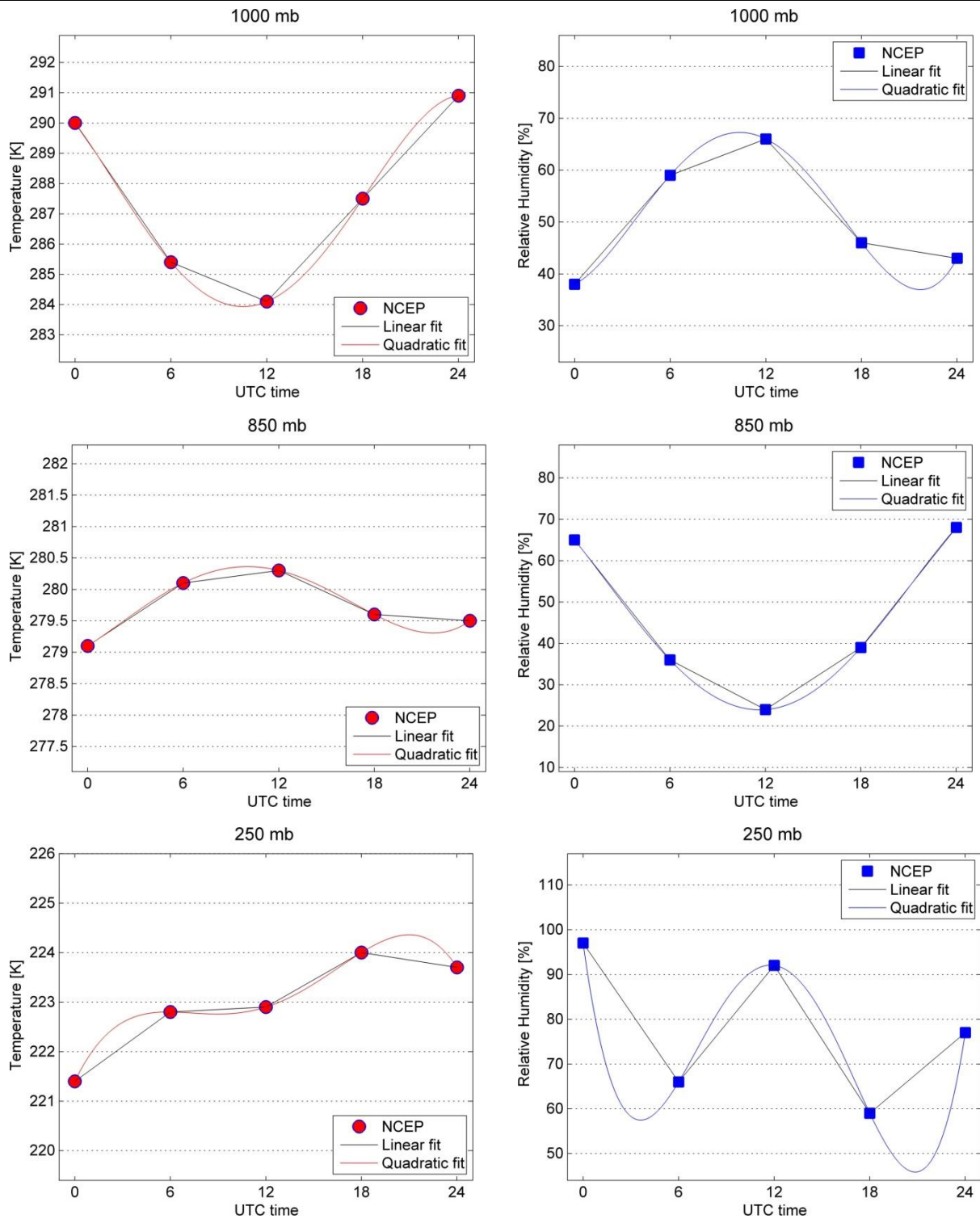


Figure 6: An example showing temporal interpolation of air temperature (left panels) and relative humidity (right panels) data from the NCEP GDAS product over Los Angeles, CA at different atmospheric levels from surface to the stratosphere. A linear and a constrained quadratic fit is used for data at 0, 6, 12, 18 UTC and 0 UTC on the following day. The results indicate that a quadratic fit is optimal for fitting air temperature data in the boundary layer and mid-troposphere, but that a linear fit is more representative at higher levels. This is also true for the relative humidity.

3.3.2 Profile Vertical and Horizontal Interpolation

A study has been conducted to develop and test different interpolation schemes using NWP data and evaluate their impact on the retrieved LST (Cook 2014). The methodologies have been developed and tested using only the NCEP North American Regional Reanalysis (NARR) data set defined over North America only (Mesinger et al. 2006). These methodologies will be adapted and used for interpolation of GEOS5 data required by SBG. The approach generates the radiative transfer parameters, τ_λ , L_λ^\downarrow , and L_λ^\uparrow (Eq. 1) at each elevation for each model grid point for the scene. Generating the radiative transfer parameters at a set of elevations at each grid point results in a three- dimensional (spatial and height) cube of data encompassing the entire scene. The radiative transfer parameters are linearly interpolated to the appropriate elevation at each of the model grid points, illustrated in Figure 7a, and these resulting parameters are interpolated to the appropriate pixel locations using Shepard’s inverse distance interpolation method, illustrated in Figure 7b.

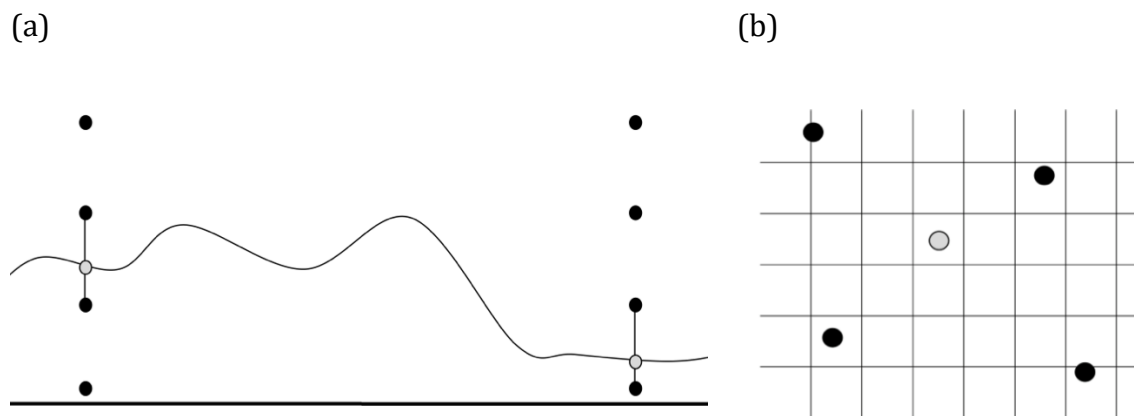


Figure 7: a) Illustration of interpolation in elevation. The black circles represent elevations at which the NWP profiles are defined. b) Illustration of spatial interpolation. The grid represents the layout of the pixels and the black circles the NWP points (not to scale). The radiative transfer parameters values at the four pertinent NWP points are interpolated to the location of the current pixel, represented by the gray circle.

3.4 Radiative Transfer Sensitivity Analysis

The accuracy of the atmospheric correction technique proposed relies on the accuracy of the input variables to the model, such as air temperature, relative humidity, and ozone. The combined uncertainties of these input variables need to be known if an estimate of the radiative transfer accuracy is to be estimated. These errors can be band dependent, since different channels have different absorbing features and they are also dependent on absolute accuracy of the input profile data at different levels. The final uncertainty introduced is the accuracy of the radiative transfer model itself; however, this is expected to be small.

To perform the analysis, four primary input geophysical parameters were input to MODTRAN 5.2, and each parameter was changed sequentially in order to estimate the corresponding percent change in radiance (Palluconi et al. 1999). These geophysical parameters were air temperature, relative humidity, and ozone. Two different atmospheres were chosen, a standard tropical atmosphere and a mid-latitude summer atmosphere. These two simulated atmospheres should capture realistic errors we expect to see in humid conditions.

Typical values for current NWP accuracies (e.g., GEOS5, ECMWF) of air temperature and relative humidity retrievals in the boundary layer were used for the perturbations: 1) air temperature of 2 K, 2) relative humidity of 20%, 3) ozone was doubled. Table 4 shows the percent changes in simulated SBG brightness temperatures for bands MIR-1 (4.0 μm) and TIR 1 (8.32 μm), 3 (9.07 μm), and 5 (10.3 μm) for changes in input geophysical parameters. SBG TIR band 1 falls closest to the strong water vapor absorption region below about 8 μm and is therefore most sensitive to perturbations in relative humidity. The temperature perturbations have similar effects for all bands with brightness temperature increases of 1-2 K for a +2K perturbation in tropospheric air temperature, but are lowest for TIR band 1 as a result of the

higher water vapor sensitivity. Doubling the ozone results in a much larger sensitivity for TIR band 3, since its band position around 9 microns falls within the ozone symmetrical normal vibration mode at 1103 cm⁻¹ (~9 micron) in addition to the primary mode which is a large asymmetric stretch at 1042 cm⁻¹ (9.6 micron) that can easily be seen as a large absorption feature (e.g. see Figure 1). Changing the aerosol visibility from rural to urban had a small effect on each band but was largest for band 5. Generally the radiance in the thermal infrared region is insensitive to aerosols in the troposphere so, for the most part, a climatology-based estimate of aerosols would be sufficient. However, when stratospheric aerosol amounts increase substantially due to volcanic eruptions, for example, then aerosols amounts from future NASA remote-sensing missions such as ACE and GEO-CAPE would need to be taken into account.

It should also be noted, as discussed in Palluconi et al. (1999), that in reality these types of errors may have different signs, change with altitude, and/or have cross-cancellation between the parameters. As a result, it is difficult to quantify the exact error budget for the radiative transfer calculation; however, what we do know is that the challenging cases will involve warm and humid atmospheres where distributions of atmospheric water vapor are the most uncertain.

Table 5: Percent changes in simulated SBG brightness temperatures for bands MIR-1 (4.0 μm) and TIR 1 (8.32 μm), 3 (9.07 μm), and 5 (10.3 μm) for changes in input geophysical parameters.

Geophysical Parameter	Parameter change	% Change in Brightness Temperature (K) (Mid-lat Summer Atmosphere)				% Change in Brightness Temperature (K) (Tropical)			
		MIR-1	TIR-1	TIR-3	TIR- 5	MIR-1	TIR-1	TIR-3	TIR-5
Air Temperature	+2 K	1.99	1.20	1.59	1.41	1.98	1.03	1.41	1.18
Relative Humidity	+20%	-0.09	-1.41	-1.04	-1.30	-0.11	-1.74	-1.43	-1.79
Ozone	+100%	-0.00	-0.05	-1.05	-0.25	-0.00	-0.05	-1.12	-0.23

3.5 Temperature and Emissivity Separation Approaches

The radiance in the TIR atmospheric window (8–13 μm) is dependent on the temperature and emissivity of the surface being observed. Even if the atmospheric properties (water vapor and air temperature) are well known and can be removed from equation (1), the problem of retrieving surface temperature and emissivity from multispectral measurements is still a non-deterministic process. This is because the total number of measurements available (N bands) is always less than the number of variables to be solved for (emissivity in N bands and one surface temperature). Therefore, no retrieval will ever do a perfect job of separation, with the consequence that errors in temperature and emissivity may co-vary. If the surface can be approximated as Lambertian (isotropic) and the emissivity is assigned *a priori* from a land cover classification, then the problem becomes deterministic with only the surface temperature being the unknown variable. Examples of such cases would be over ocean, ice, or densely vegetated scenes where the emissivity is known and spectrally flat in all bands. Another deterministic approach is the single-band inversion approach. If the atmospheric parameters are known in equation (1), then the temperature can also be solved for using a single band, usually in the clearest region of the window ($\sim 11 \mu\text{m}$). Deterministic approaches are usually employed with sensors that have two or three bands in the TIR region, while non-deterministic approaches are applied to multispectral sensors so that spectral variations in the retrieved emissivity can be related to surface composition and cover, in addition to retrieving the surface temperature. For ECOSTRESS, a non-deterministic approach will be used, as spectral emissivity will need to be determined physically, along with temperature, in order to help answer the science questions outlined previously in section 3.

3.5.1 Deterministic Approaches

3.5.1.1 *Split-window Algorithms*

The most common deterministic approach can be employed without having to explicitly solve the radiative transfer equation. Two or more bands are employed in the window region (typically 10.5–12 μm), and atmospheric effects are compensated for by the differential absorption characteristics from the two bands. This approach is used with much success over oceans to compute the SST (Brown and Minnett 1999), as the emissivity of water is well known (Masuda et al. 1988). Variations of this method over land include the split-window (SW) approach (Coll and Caselles 1997; Prata 1994; Price 1984; Wan and Dozier 1996; Yu et al. 2008), the multichannel algorithm (Deschamps and Phulpin 1980), and the dual-angle algorithm (Barton et al. 1989). Over land, the assumption is that emissivities in the split-window bands being used are stable and well known and can be assigned using a land cover classification map (Snyder et al. 1998). However, this assumption introduces large errors over barren surfaces where much larger variations in emissivity are found due to the presence of large amounts of exposed rock or soil often with abundant silicates (Hulley and Hook 2009a). Land cover classification maps typically use VNIR data for assignment of various classes. This method may work for most vegetation types and over water surfaces but, because VNIR reflectances correspond predominately to Fe oxides and OH^- and not to the Si-O bond over barren areas, there is little or no correlation with silicate mineralogy features in thermal infrared data. This is why, in most classification maps, only one bare land class is specified (barren). This type of approach will not be used for the SBG standard algorithm over land, but may be employed over coastal oceans and deep oceans, for the following reasons:

1. The emissivity of the land surface is in general heterogeneous and is dependent on many factors including surface soil moisture, vegetation cover changes, and surface compositional changes, which are not characterized by classification maps.
2. Split-window algorithms are inherently very sensitive to measurement noise between bands.
3. Classification leads to sharp discontinuities and contours in the data between different class types. This violates one of the goals of SBG in producing seamless images.
4. Temperature inaccuracies are difficult to quantify over geologic surfaces where constant emissivities are assigned.

3.5.1.2 Single-band Inversion

If the atmosphere is known, along with an estimate of the emissivity, then equation (1) can be inverted to retrieve the surface temperature using one band. Theoretically, any band used should retrieve the same temperature, but uncertainties in the atmospheric correction will result in subtle differences as different bands have stronger atmospheric absorption features than others which may be imperfectly corrected for atmospheric absorption. For example, a band near 8 μm will have larger dependence on water vapor, while the 9–10- μm region will be more susceptible to ozone absorption. Jimenez-Munoz and Sobrino (2010) applied this method to ASTER data by using atmospheric functions (AFs) to account for atmospheric effects. The AFs can be computed by the radiative transfer equation or empirically given the total water vapor content. The clearest ASTER band (13 or 14) was used to retrieve the temperature, with the emissivity determined using an NDVI fractional vegetation cover approach. A similar procedure has been proposed to retrieve temperatures from the Landsat TIR band 6 on ETM+ and TM sensors (Li et al. 2004). The single-band inversion method will not be used for SBG for the following reasons:

1. One of the goals of SBG science will be to retrieve the spectral emissivity of geologic surfaces for compositional analysis. This will not be possible with the single-band approach, which assigns emissivity based on land cover type and vegetation fraction.
2. Estimating emissivity from NDVI-derived vegetation cover fraction over arid and semi-arid regions will introduce errors in the LST because NDVI is responsive only to chlorophyll active vegetation, and does not correlate well with senescent vegetation (e.g., shrublands).
3. Only one-band emissivity is solved for the single-band inversion approach. SBG will be a multispectral retrieval approach.

3.5.2 Non-deterministic Approaches

In non-deterministic approaches, the temperature and emissivity is solved using an additional constraint or extra degree of freedom that is independent of the data source. These types of solutions are also rarely perfect because the additional constraint will always introduce an additional level of uncertainty, however, they work well over all surfaces (including arid and semi arid) and can automatically account for changes in the surface e.g. due to fire or moisture. First, we introduce two well-known approaches, the day/night and TISI algorithms, followed by an examination of the algorithms and methods that led up to establishment of the TES algorithm.

3.5.2.1 Day/Night Algorithm

The constraint in the day/night algorithm capitalizes on the fact that the emissivity is an intrinsic property of the surface and should not change from day- to nighttime observations. The day/night algorithm is currently used to retrieve temperature/emissivity from MODIS data in the MOD11B1 product (Wan and Li 1997). The method relies on two measurements (day and night), and the theory is as follows: Two observations in N bands produces 2N observations, with the unknown variables being N-band emissivities, a day- and nighttime surface temperature, four

atmospheric variables (day and night air temperature and water vapor), and an anisotropic factor, giving $N + 7$ variables. In order to make the problem deterministic, the following conditions must be met: $2N \geq N + 7$, or $N \geq 7$. For the MODIS algorithm, this can be satisfied by using bands 20, 22, 23, 29, 31–33. Although this method is theoretically sound, the retrieval is complicated by the fact that two clear, independent observations are needed (preferably close in time) and the pixels from day and night should be perfectly co-registered. Errors may be introduced when the emissivity changes from day to night observation (e.g., due to condensation or dew), and from undetected nighttime cloud. In addition, the method relies on very precise co-registration between the day- and nighttime pixel.

3.5.2.2 Temperature Emissivity Separation Approaches

During research activities leading up to the ASTER mission, the ASTER Temperature Emissivity Working Group (TEWG) was established in order to examine the performance of existing non-deterministic algorithms and select one suitable for retrieving the most accurate temperature and/or emissivity over the entire range of terrestrial surfaces. This led to development of the TES algorithm, which ended up being a hybrid algorithm that capitalized on the strengths of previous algorithms. In Gillespie et al. (1999), ten inversion algorithms were outlined and tested, leading up to development of TES. For all ten algorithms, an independent atmospheric correction was necessary. The ten algorithms were as follows:

1. Alpha-derived emissivity (ADE) method
2. Classification method
3. Day-Night measurement
4. Emissivity bounds method

5. Graybody emissivity method
6. Mean-MMD method (MMD)
7. Model emissivity method
8. Normalized emissivity method (NEM)
9. Ratio Algorithm
10. Split-window algorithm

In this document, we will briefly discuss a few of the algorithms but will not expand upon any of them in great detail. The day-night measurement (3), classification (2), and split-window (10) algorithms have already been discussed in section 4.2.1. A detailed description of all ten algorithms is available in Gillespie et al. (1999). The various constraints proposed in these algorithms either determine spectral shape but not temperature, use multiple observations (day and night), assume a value for emissivity and calculate temperature, assume a spectral shape, or assume a relationship between spectral shape and minimum emissivity.

The normalized emissivity method (NEM) removes the downwelling sky irradiance component by assuming an ϵ_{max} of 0.99. Temperature is then estimated by inverting the Planck function and a new emissivity found. This process is repeated until successive changes in the estimated surface radiances are small. This method in itself was not found to be suitable for ASTER because temperature inaccuracies tended to be high (>3 K) and the emissivities had incorrect spectral shapes. Other approaches have used a model to estimate emissivity at one wavelength (Lyon 1965) or required that the emissivity be the same at two wavelengths (Barducci and Pippi 1996). This introduces problems for multispectral data with more than 5 bands.

The ADE method (Hook et al. 1992; Kealy et al. 1990; Kealy and Hook 1993) is based on the alpha residual method that preserves emissivity spectral shape but not amplitude or temperature. The constraint introduced uses an empirical relationship between spectral contrast and average emissivity to restore the amplitude of the alpha-residual spectrum and to compute temperature. The average emissivity was used in the relationship to minimize band-to-band calibration errors. The TEWG used this key feature of the ADE method in TES, although the minimum emissivity instead of average emissivity was used in the empirical relationship (Matsunaga 1994). The ADE itself was not fully employed for two primary reasons as discussed in Gillespie et al. (1999): 1) ADE uses Wien's approximation, $\exp(x) - 1 = \exp(x)$, which introduces a noticeable "tilt" in the residual spectra that gets transferred to the final emissivity spectra; and 2) This issue was easily fixed in the hybrid version of TES.

Lastly, the temperature-independent spectral indices (TISI) approach (Becker and Li 1990) computes relative emissivities from power-scaled brightness temperatures. TISI, however, is band-dependent and only recovers spectral shape; furthermore, the values are non unique. To retrieve actual emissivities, additional information or assumptions are needed. Other algorithms, which only retrieve spectral shape, are the thermal log and alpha residual approach (Hook et al. 1992) and spectral emissivity ratios (Watson 1992; Watson et al. 1990). Neither of these were considered because they do not recover temperature or actual emissivity values.

4 Temperature Emissivity Separation (TES) Algorithm

The final TES algorithm proposed by the ASTER TEWG combined some core features from previous algorithms and, at the same time, improved on them. TES combines the NEM, the ratio, and the minimum-maximum difference (MMD) algorithm to retrieve temperature and a

full emissivity spectrum. The NEM algorithm is used to estimate temperature and iteratively remove the sky irradiance, from which an emissivity spectrum is calculated, and then ratioed to their mean value in the ratio algorithm. At this point, only the shape of the emissivity spectrum is preserved, but not the amplitude. In order to compute an accurate temperature, the correct amplitude is then found by relating the minimum emissivity to the spectral contrast (MMD). Once the correct emissivities are found, a final temperature can be calculated with the maximum emissivity value. Additional improvements involve a refinement of ϵ_{max} in the NEM module and refining the correction for sky irradiance using the ϵ_{min} -MMD final emissivity and temperature values. Finally, a quality assurance (QA) data image is produced that partly depends on outputs from TES such as convergence, final ϵ_{max} , atmospheric humidity, and proximity to clouds. More detailed discussion of QA is included later in this document.

Numerical modeling studies performed by the ASTER TEWG showed that TES can recover temperatures to within 1.5 K and emissivities to within 0.015 over most scenes, assuming well calibrated, accurate radiometric measurements (Gillespie et al. 1998).

4.1 Data Inputs

Inputs to the TES algorithm are the surface radiance, $L_{s,i}$, given by equation (4) (at-sensor radiance corrected for transmittance and path radiance), and downwelling sky irradiance term, L_{λ}^{\downarrow} , which is computed from the atmospheric correction algorithm using a radiative transfer model such as MODTRAN. Both the surface radiance and sky irradiance will be output as a separate product. The surface radiance is primarily used as a diagnostic tool for monitoring changes in Earth's surface composition. Before the surface radiance is estimated using equation (4), the accuracy of the atmospheric parameters, L_{λ}^{\downarrow} , $\tau_{\lambda}(\theta)$, $L_{\lambda}^{\uparrow}(\theta)$, is improved upon using a

water vapor scaling (WVS) method (Tonooka 2005) on a band-by-band basis for each observation using an extended multi-channel/water vapor dependent (EMC/WVD) algorithm (for more details, see SBG Surface Radiance ATBD).

4.2 TES Limitations

As with any retrieval algorithm, limitations exist that depend on measurement accuracy, model errors, and incomplete characterization of atmospheric effects. The largest source of inaccuracy currently for ASTER data is the residual effect of incomplete atmospheric correction. Measurement accuracy and precision contribute to less of a degree. This problem is compounded for graybodies, which have low spectral contrast and are therefore more prone to errors in "apparent" MMD, which is overestimated due to residual sensor noise and incomplete atmospheric correction. A threshold classifier was introduced by the TEWG to partly solve this problem over graybody surfaces. Instead of using the calibration curve to estimate ϵ_{min} from MMD, a value of $\epsilon_{min}=0.983$ was automatically assigned when the spectral contrast or MMD in emissivity was smaller than 0.03 for graybody surfaces (e.g., water, vegetation). However, this caused artificial step discontinuities in emissivity between vegetated and arid areas.

At the request of users, two parameter changes were made to the ASTER TES algorithm on August 1, 2007, first described in Gustafson et al. (2006). Firstly, the threshold classifier was removed as it caused contours and artificial boundaries in the images that users could not tolerate in their analysis. The consequence of removing the threshold classifier was a smoother appearance for all images but at the cost of TES underestimating the emissivity of graybody scenes, such as water by up to 3% and vegetation by up to 2% (Hulley et al. 2008). The second parameter change removed the iterative correction for reflected downwelling radiation, which

also frequently failed due to inaccurate atmospheric corrections (Gustafson et al. 2006). Using only the first iteration resulted in improved spectral shape and performance of TES.

4.3 TES Processing Flow

Figure 8 shows the processing flow diagram for the generation of the cloud masks, land-leaving radiance, VNIR reflectances, and TES temperature and emissivity, while Figure 9 shows a more detailed processing flow of the TES algorithm itself. Each of the steps will be presented in sufficient detail in the following section, allowing users to regenerate the code. TES uses input image data of surface radiance, $L_{s,i}$, and sky irradiance, L_{λ}^{\downarrow} , to solve the TIR radiative transfer equation. The output images will consist of seven emissivity images (ϵ_i) corresponding to SBG MIR band 1 and TIR bands 1-6, and one surface temperature image (T). Emissivity will not be retrieved for MIR band 2 (4.8 micron) due to its strong CO₂ absorption features.

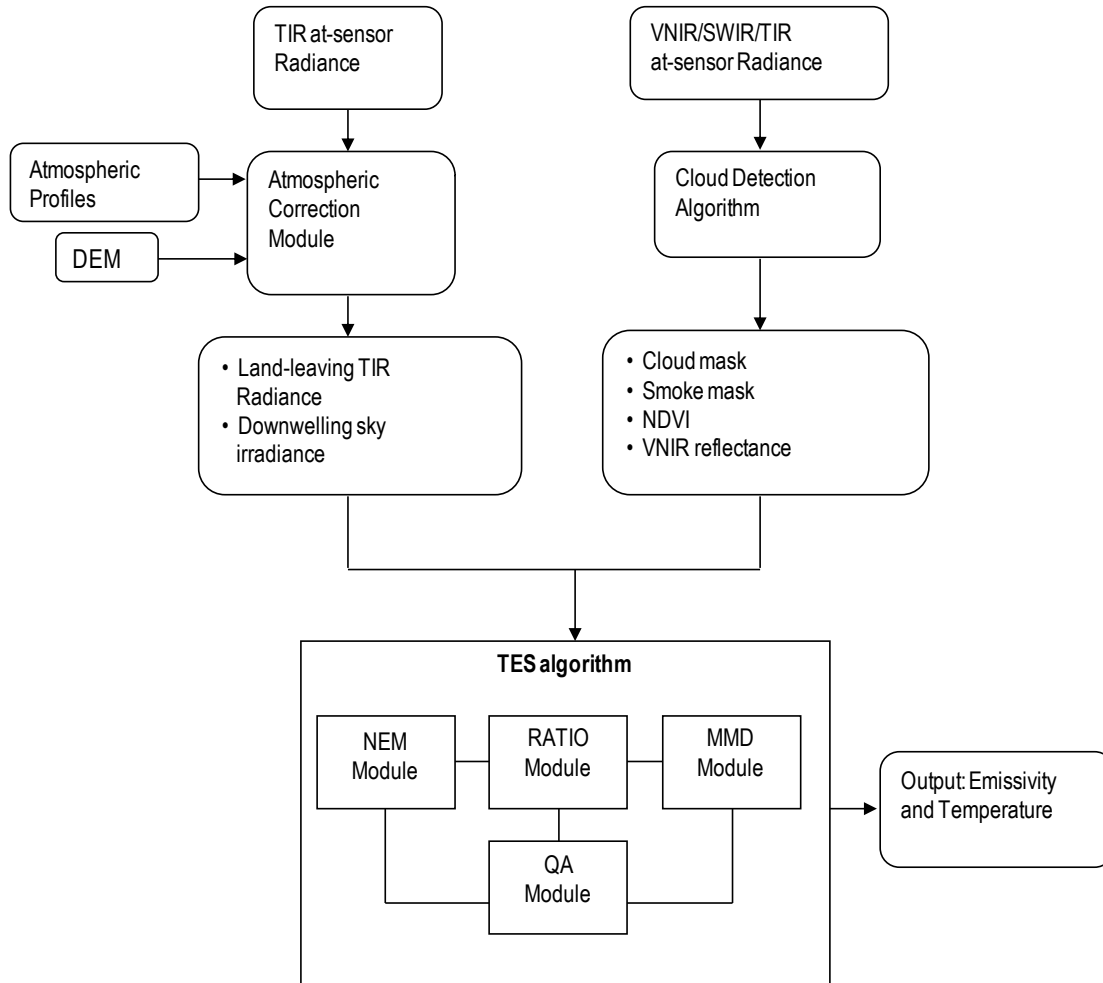


Figure 8. Flow diagram showing all steps in the retrieval process in generating the SBG land surface temperature and emissivity product starting with thermal infrared (TIR) at-sensor radiances and progressing through atmospheric correction, cloud detection, and the temperature emissivity separation (TES) algorithm.

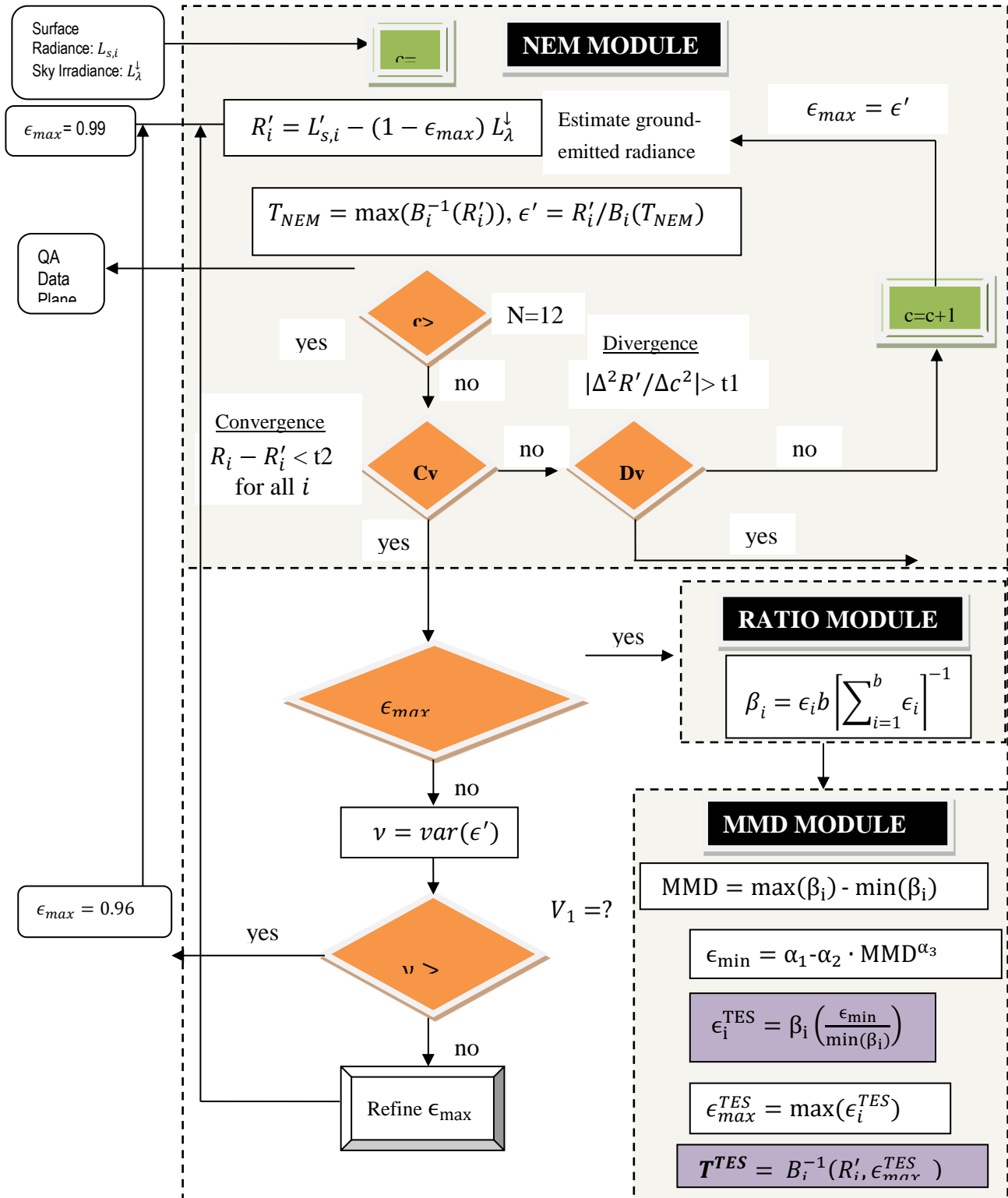


Figure 9. Flow diagram of the temperature emissivity separation (TES) algorithm in its entirety, including the NEM, RATIO and MMD modules. Details are included in the text, including information about the refinement of ϵ_{max} .

4.4 NEM Module

The normalized emissivity method (NEM) builds upon the model emissivity algorithm (Lyon 1965) by allowing the initial ϵ_{max} value to be consistent for all wavelengths. The role of NEM is to compute the surface kinetic temperature, T, and a correct shape for the emissivity spectrum. An initial value of 0.99 is set for ϵ_{max} , which is typical for most vegetated surfaces, snow, and water. For geologic materials such as rocks and sand, ϵ_{max} values are set lower than this, typically 0.96, and this value remains fixed. For all other surface types, a modification to the original NEM allows for optimization of ϵ_{max} using an empirically based process. For the majority of materials in the ECOSTRESS spectral library, a typical range for ϵ_{max} is $0.94 < \epsilon_{max} < 1.0$. Therefore, for a material at 300 K, the maximum errors that NEM temperatures should have are $\sim \pm 1.5$ K, assuming the reflected sky irradiance has been estimated correctly.

4.5 Removing Downwelling Sky Irradiance

Generally the effects of sky irradiance are small with typical corrections of < 1 K (Gillespie et al. 1998). However, the contribution becomes larger for pixels with low emissivity (high reflectance) or in humid conditions when the sky is warmer than the surface. Over graybody surfaces (water and vegetation), the effects are small because of their low reflectivity in all bands. The first step of the NEM module is to estimate ground-emitted radiance, which is found by subtracting the reflected sky irradiance from the surface radiance term:

$$R_i = L'_{s,i} - (1 - \epsilon_{max}) L_{\lambda}^{\downarrow} \quad (6)$$

The NEM temperature, which we call T_{NEM} , is then estimated by inverting the Planck function for each band using ϵ_{max} and the ground-emitted radiance and then taking the maximum of those temperatures. The maximum temperature will most likely be closest to the actual surface temperature in the presence of uncompensated atmospheric effects.

$$T_i = \frac{c_2}{\lambda_i} \left(\ln \left(\frac{c_1 \epsilon_{max}}{\pi R_i \lambda_i^5} + 1 \right) \right)^{-1} \quad (7)$$

$$T_{NEM} = \max(T_i) \quad (8)$$

The NEM emissivity spectrum is then calculated as the ratio of emitted radiance to that of a blackbody with a temperature estimated by T_{NEM} :

$$\epsilon'_i = \frac{R_i}{B_i(T_{NEM})} \quad (9)$$

The new emissivity spectrum is then used to re-calculate $R'_i = L'_{s,i} - (1 - \epsilon'_i) L_{\lambda}^{\downarrow}$, and the process is repeated until convergence, which is determined if the change in R_i between steps is less than a set threshold, t_2 , which is set as the radiance equivalent to NE Δ T of the sensor. The process is stopped if the number of iterations exceeds a limit N, set to 12. Execution of the NEM module is also aborted if the slope of R_i versus iteration, c , increases such that $|\Delta^2 R' / \Delta c^2| > t_1$, where t_1 is also set to radiance equivalent of NE Δ T for the sensor (still to be determined for SBG). In this case, correction is not possible, TES is aborted, and NEM values of ϵ_i and T_{NEM} are reported in the QA data plane, along with an error flag. TES is also aborted and an error flag recorded if, for any iteration, the values of ϵ_i fall out of reasonable limits, set to $0.5 < \epsilon_i < 1.0$. See Figure 11 for a detailed description of these steps.

4.6 Refinement of ϵ_{max}

Most pixels at SBG resolution (60 m) will contain a mixed cover type consisting of vegetation and soil, rock and water. The effective maximum emissivity for such pixels will therefore vary across the scene and depend on the fractional contribution of each cover type. For these cases, the initial $\epsilon_{max} = 0.99$ may be set to high and refinement of ϵ_{max} is necessary to

improve accuracy of T_{NEM} . The optimal value for ϵ_{max} minimizes the variance, ν , of the NEM calculated emissivities, ϵ_i . The optimization of ϵ_{max} is only useful for pixels with low emissivity contrast (near graybody surfaces) and therefore is only executed if the variance for $\epsilon_{max} = 0.99$ is less than an empirically determined threshold (e.g., $V_1 = 1.7 \times 10^{-4}$ for ASTER) (Gillespie et al. 1998). If the variance is greater than V_1 , then the pixel is assumed to predominately consist of either rock or soil. For this case, ϵ_{max} is reset to 0.96, which is a good first guess for most rocks and soils in the ECOSTRESS spectral library, which typically fall between the 0.94 and 0.99 range. If the first condition is met, and the pixel is a near-graybody, then values for ϵ_{max} of 0.92, 0.95, 0.97, and 0.99 are used to compute the variance for each corresponding NEM emissivity spectrum. A plot of variance ν versus each ϵ_{max} value results in an upward-facing parabola with the optimal ϵ_{max} value determined by the minimum of the parabola curve in the range $0.9 < \epsilon_{max} < 1.0$. This minimum is set to a new ϵ_{max} value, and the NEM module is executed again to compute a new T_{NEM} . Further tests are used to see if a reliable solution can be found for the refined ϵ_{max} . If the parabola is too flat, or too steep, then refinement is aborted and the original ϵ_{max} value is used. The steepness condition is met if the first derivative (slope of ν vs. ϵ_{max}) is greater than a set threshold (e.g., $V_2 = 1.0 \times 10^{-3}$ for ASTER) and the flatness condition is met if the second derivative is less than a set threshold (e.g., $V_3 = 1.0 \times 10^{-3}$ for ASTER). Finally, if the minimum ϵ_{max} corresponds to a very low ν , then the spectrum is essentially flat (graybody) and the original $\epsilon_{max} = 0.99$ is used. This condition is met if $\nu_{min} < V_4$ (e.g. $V_4 = 1.0 \times 10^{-4}$ for ASTER). These thresholds will need to be refined for the SBG bands and determined empirically.

4.7 Ratio Module

In the ratio module, the NEM emissivities are ratioed to their average value to calculate a β_i spectrum as follows:

$$\beta_i = \frac{\epsilon_i}{\bar{\epsilon}} \quad (10)$$

Typical ranges for the β_i emissivities are $0.75 < \beta_i < 1.32$, given that typical emissivities range from 0.7 to 1.0. Errors in the β_i spectrum due to incorrect NEM temperatures are generally systematic.

4.8 MMD Module

In the minimum-maximum difference (MMD) module, the β_i emissivities are scaled to an actual emissivity spectrum using information from the spectral contrast or MMD of the β_i spectrum. The MMD can then be related to the minimum emissivity, ϵ_{min} , in the spectrum using an empirical relationship determined from lab measurements of a variety of different spectra, including rocks, soils, vegetation, water, and snow/ice. From ϵ_{min} , the actual emissivity spectrum can be found by re-scaling the β_i spectrum. First, the MMD of the β_i spectrum is found by:

$$MMD = \max(\beta_i) - \min(\beta_i) \quad (11)$$

Then MMD can be related to ϵ_{min} using a power-law relationship:

$$\epsilon_{min} = \alpha_1 - \alpha_2 MMD^{\alpha_3}, \quad (12)$$

where α_j are coefficients that are obtained by regression using lab measurements. For the six SBG TIR bands between 8 and 12 μm (shown in Figure 1), the values for the coefficients were calculated as $\alpha_1 = 0.9929$, $\alpha_2 = 0.7453$, and $\alpha_3 = 0.8149$. The TES emissivities are then calculated by re-scaling the β_i emissivities:

$$\epsilon_i^{TES} = \beta_i \left(\frac{\epsilon_{min}}{\min(\beta_i)} \right) \quad (13)$$

For pixels with low spectral contrast (e.g., graybody surfaces), the accuracy of MMD calculated from TES is compromised and approaches a value that depends on measurement error and residual errors from incomplete atmospheric correction. For ASTER, which has a NE Δ T of 0.3 K at 300 K, measurement error contributes to the apparent contrast, and a method was explored to correct the apparent MMD using Monte Carlo simulations. For SBG (NE Δ T of ~0.1-0.2 K per band), we expect measurement errors to be minimal and atmospheric effects to be the largest contribution to MMD errors. A further problem for graybody surfaces is a loss of precision for low MMD values. This is due to the shape of the power-law curve of ϵ_{min} vs. MMD at low MMD values, where small changes in MMD can lead to large changes in ϵ_{min} . To address these issues, the ASTER TEWG initially proposed a threshold classifier for graybody surfaces. If MMD < 0.03, the value of ϵ_{min} in equation (13) was set to 0.983, a value typical for water and most vegetated surfaces. However, this classification was later abandoned as it introduced large step discontinuities in most images (e.g., from vegetation to mixed-cover types).

The consequence of removing the threshold classifier was that over graybody surfaces errors in emissivity could range from 0.01 to 0.05 (0.5 K to 3 K) due to measurement error and residuals errors from atmospheric correction (Gustafson et al. 2006; Hulley and Hook 2009b). For SBG, we expect to use original TES without classification and use the WVS method to correct the atmospheric parameters on a pixel-by-pixel basis.

For bare surfaces (rocks, soils, and sand), the error in NEM calculated T may be as much as 2–3 K, assuming a surface at 340 K due to the fixed assumption of $\epsilon_{max} = 0.96$. This error can be corrected by recalculating T using the TES retrieved maximum emissivity, ϵ_{max}^{TES} , and the

atmospherically corrected radiances, R_i . The maximum emissivity used as correction for reflected L_λ^\downarrow will be minimal.

$$T^{TES} = \frac{c_2}{\lambda_{max}} \left(\ln \left(\frac{c_1 \epsilon_{max}^{TES}}{\pi R_i \lambda_{max}^5} + 1 \right) \right)^{-1} \quad (14)$$

An example LST and emissivity simulated SBG scene are shown in Figures 10 and 11 respectively. The SBG scenes was simulated from MASTER data acquired on 30 January 2018 over Kilauea, Hawaii. TES was first applied to similar MASTER bands as SBG to retrieve the LST and emissivity, and then a regression based technique was used to adjust the MASTER emissivity bands for the equivalent SBG bands shown in Figure 1. Bare areas of rock and soil and the Kilauea lava flow on the southeast side have emissivities <0.85 in the 9 micron band, while graybody surfaces such as dense vegetation or water have higher emissivities >0.95 . Figure 11 shows a simulated SBG emissivity scene for the same MASTER line for band TIR-3 (9 micron).

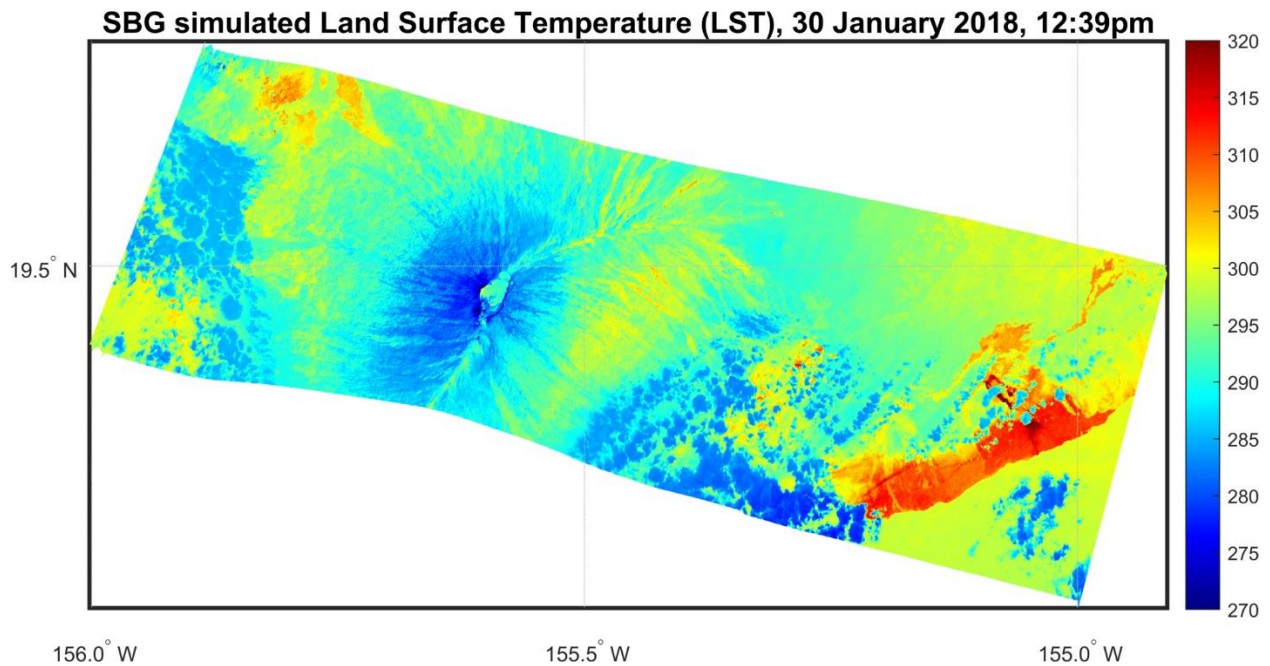


Figure 10. SBG simulated LST generated from a MASTER scene on 30 January 2018 over Mauna Loa and Kilauea volcanoes in Hawaii.

using various combinations and numbers of different spectra (e.g., Australian rocks, airborne data, and a subset of 31 spectra from Salisbury), and all yielded very similar results to the original 86 spectra.

For SBG, the original 86 spectra were updated to include additional sand spectra used to validate the North American ASTER Land Surface Emissivity Database (NAALSED) (Hulley and Hook 2009b) and additional spectra for vegetation from the MODIS spectral library and ASTER spectral library v2.0, giving a total of 150 spectra. The data were convolved to the nominal SBG bands and ϵ_{min} and β_i spectra calculated for each sample. The MMD for each spectra was then calculated from the β_i spectra and regressed to the ϵ_{min} values. The relationship follows a simple power law given by equation (7), with regression coefficients $\alpha_1 = 0.9929$, $\alpha_2 = 0.7453$, and $\alpha_3 = 0.8149$, and $R^2 = 0.989$. Figure 12 shows the power-law relationship between MMD and ϵ_{min} using the 150 lab spectra.

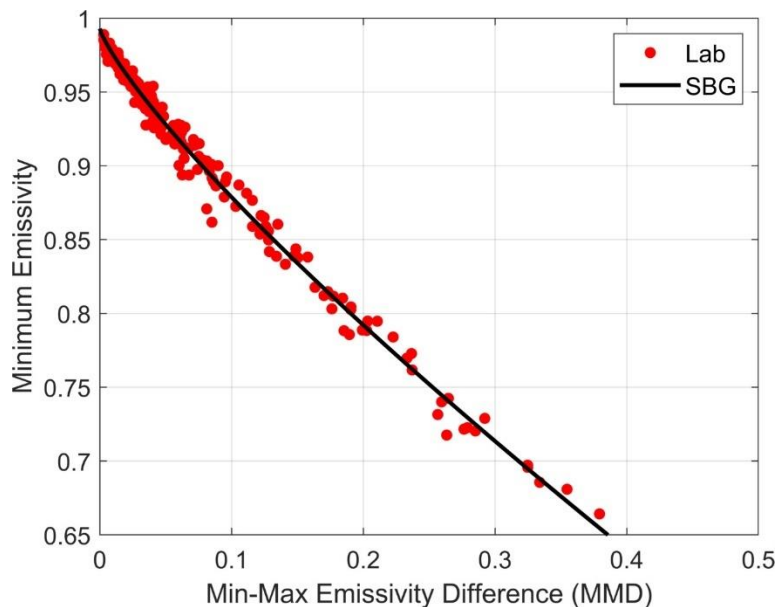


Figure 12. SBG calibration curve of minimum emissivity vs. min-max difference (MMD). The lab data (crosses) are computed from 150 spectra consisting of a broad range of terrestrial materials (rocks, sand, soil, water, vegetation, and ice).

5 Uncertainty Analysis

NASA has identified a major need to develop long-term, consistent products valid across multiple missions, with well-defined uncertainty statistics addressing specific Earth-science questions. These products are termed Earth System Data Records (ESDRs), and LST&E has been identified as an important ESDR. Currently a lack of understanding of LST&E uncertainties limits their usefulness in land surface and climate models. In this section we present results from the Temperature Emissivity Uncertainty Simulator (TEUSim) that has been developed to quantify and model uncertainties for a variety of TIR sensors and LST algorithms (Hulley et al. 2012b). Using the simulator, uncertainties were estimated for the L2 products of SBG using a 6-band TES approach. These uncertainties will be parameterized according to view angle and estimated total column water vapor for eventual application to real-time SBG L2 data on a pixel by pixel basis.

5.1 The Temperature and Emissivity Uncertainty Simulator (TEUSim)

The TEUSim was developed for simulating LST&E uncertainties from various sources of error for the TES and SW algorithms in a rigorous manner for any appropriate TIR sensor (see Figure 13). These include random errors (e.g. instrument noise), systematic errors (e.g. calibration), and spatio-temporally correlated errors (e.g. atmospheric correction). The MODTRAN v6 radiative transfer model is used for the simulations with a global set of radiosonde profiles and surface emissivity spectra representing a broad range of atmospheric conditions and a wide variety of surface types. This approach allows the retrieval algorithm to be easily evaluated under realistic but challenging combinations of surface/atmospheric conditions. The TEUSim is designed to separately quantify error contributions from the following potential sources:

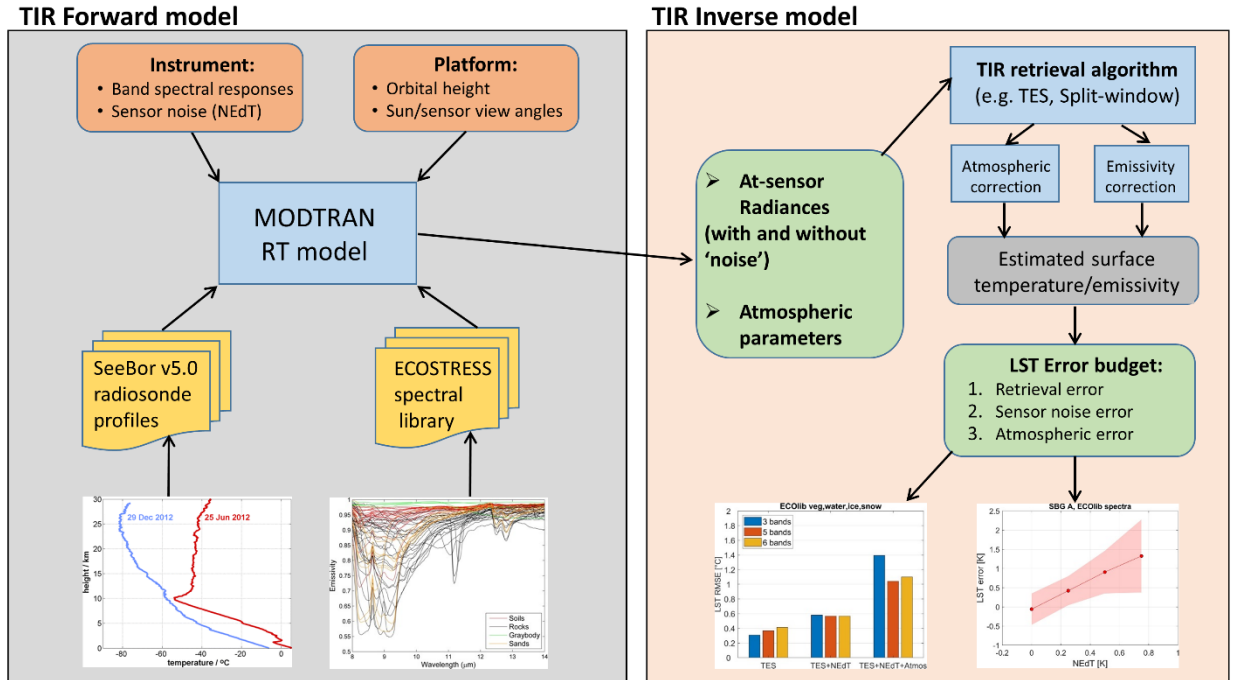


Figure 13. Schematic of the Temperature Emissivity Uncertainty Simulator (TEUSim) forward (left) and inverse (right) models describing the inputs, outputs and general flow for generating the LST error budget.

1. Instrument noise (NEdT)
2. Algorithm (Model)
3. Atmospheric correction
4. Undetected cloud
5. Calibration

The results presented in this study will focus on the first three of these error sources: instrument noise, algorithm, and atmospheric correction. The effects of cloud and calibration issues will be quantified in orbit once enough data is acquired.

5.2 Atmospheric Profiles

The TEUSim uses a global simulation model with input atmospheric data from the SeeBor V5.0 radiosounding database (Borbas et al. 2005). The SeeBor data consist of 15,704 profiles of uniformly distributed global atmospheric soundings temperature, moisture, and ozone at 101 pressure levels for clear sky conditions, acquired both day and night in order to capture the full-scale natural atmospheric variability (Figure 14).

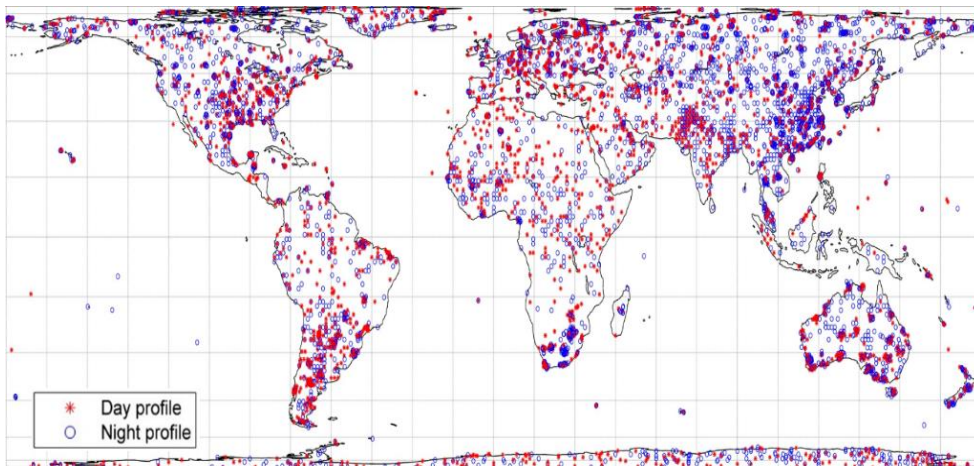


Figure 14. Locations of the 15,704 day and nighttime atmospheric soundings of temperature, moisture, and ozone of from the SeeBor V5.0 radiosounding database.

5.3 Radiative Transfer Model

In TEUSim the latest version of MODTRAN (v6) was used for the radiative transfer calculations. MODTRAN 6 uses an improved molecular band model, termed the Spectrally Enhanced Resolution MODTRAN (SERTRAN), which has a much finer spectroscopy (0.1 cm^{-1}) than previous versions ($1\text{--}2 \text{ cm}^{-1}$). This results in higher accuracy in modeling of band absorption features in the longwave TIR window regions, and comparisons with line-by-line models has shown good accuracy (Berk et al. 2005).

5.4 Surface End-Member Selection

A selection of emissivity spectra from the ECOSTRESS Spectral Library (ECOLib) (Meerdink et al. 2019) were used to define the surface spectral emission term in MODTRAN. A total of 59 spectra were chosen based on certain criteria and grouped into four surface classifications: rocks (20), soils (26), sands (9), and graybodies (4). Spectra were chosen to represent the most realistic effective emissivities observed at the remote sensing scales.

For rocks, certain spectra were removed prior to processing based on two considerations. First, samples that rarely exist as kilometer-scale, sub-aerial end-member exposures on the Earth's surface such as pyroxenite or serpentinite were eliminated. Second, and in parallel, spectrally similar samples were eliminated. Spectral similarity was defined by the location, shape, and magnitude of spectral features between 7 and 13 μm . All eliminated samples are represented in the final selection through spectrally-similar end-member types. The final rock set included 20 spectra.

ECOLib includes 49 soil spectra classified according to their taxonomy, such as Alfisol (9), Aridisol (14), Entisol (10), Inceptisol (7) and Mollisol (9). Filtering in this case was based solely on spectral similarity between each taxonomy type. The final soils set included 26 soil spectra.

A set of nine emissivity spectra collected in separate field campaigns during 2008 over large homogeneous sand dune sites in the southwestern United States in support of validation for the NAALSED v2.0 (Hulley et al. 2009a) were used for sands. The sand samples consist of a wide variety of different minerals including quartz, magnetite, feldspars, gypsum, and basalt mixed in various amounts, and represent a broad range of emissivities in the TIR as detailed in Hulley et al. (2009a).

To represent graybody surfaces, spectra of distilled water, ice, snow, and conifer were chosen from ASTlib. Four spectra were sufficient to represent this class since graybody surfaces exhibit low contrast and high emissivities. It should be noted that certain types of man-made materials were not included, such as aluminum roofs that do not occur at the spatial resolution of these sensors, but should be included for higher-spatial-resolution data sets such as those provided by airborne instruments.

5.5 Radiative Transfer Simulations

In the TEUSim, each radiosonde profile for each set of end-member spectra can be used as an input to MODTRAN, or a subset of particular types of atmospheric data and surface spectra may be used. A seasonal rural aerosol is typically assumed with standard profiles for fixed gases within MODTRAN. Gaussian viewing angles of 0° , 11.6° , 26.1° and 40.3° were used to represent the viewing geometry of SBG that will not exceed 35° . The downward sky irradiance, $L_\lambda(\theta)$, can be modeled using the path radiance, transmittance, and view angle. To simulate the downward sky irradiance in MODTRAN, the sensor target is placed a few meters above the surface, with surface emission set to zero, and view angle set at the prescribed angles above. In this configuration, the reflected downwelling sky irradiance is estimated for a given view angle. The total sky irradiance contribution for band i is then calculated by summing the contribution of all view angles over the entire hemisphere:

$$L_i^\downarrow = \int_0^{2\pi} \int_0^{\pi/2} L_i^\downarrow(\theta) \cdot \sin\theta \cdot \cos\theta \cdot d\theta \cdot d\delta \quad (15)$$

where θ is the view angle and δ is the azimuth angle. To minimize computational time, the downward sky irradiance is first modeled as a non-linear function of path radiance at nadir view using (17) (Tonooka 2001):

$$L_i^\downarrow(\gamma) = a_i + b_i \cdot L_i^\uparrow(0, \gamma) + c_i L_i^\uparrow(0, \gamma)^2 \quad (16)$$

where a_i , b_i , and c_i are regression coefficients, and $L_i^\uparrow(0, \gamma)$ is computed by:

$$L_i^\uparrow(0, \gamma) = L_i^\uparrow(\theta, \gamma) \cdot \frac{1 - \tau_i(\theta, \gamma)^{\cos\theta}}{1 - \tau_i(\theta, \gamma)} \quad (17)$$

Equations (17) and (18) were used to estimate the downwelling sky irradiance in the TEUSim results using pre-calculated regression coefficients for SBG bands. The reflected sky irradiance term is generally smaller in magnitude than the surface-emitted radiance, but needs to be taken into account, particularly on humid days when the total atmospheric water vapor content is high. The simulated LST is based on the surface air temperature of each radiosonde profile:

$$LST_{sim} = T_{air} + \delta T \quad (18)$$

where LST_{sim} and T_{air} are the simulated LST and surface air temperature. Galve et al. (2008) found a mean δT of +3 K and standard deviation of 9 K from a global study of surface-air temperature differences over land in the MODIS MOD08 and MOD11 products. We therefore defined δT as a random distribution with a mean of 3 K and a standard deviation of 9 K for each profile input to MODTRAN.

The TES algorithm uses surface radiance as input, which can be derived from the atmospheric transmittance $\tau_\lambda(\theta)$, TOA radiance $L_\lambda(\theta)$, path radiance $L_\lambda^\uparrow(\theta)$, and downward sky irradiance $L_\lambda^\downarrow(\theta)$. To calculate the various sources of error in LST&E retrievals from TES, these variables were simulated for the following conditions:

1. Perfect atmosphere (i.e., exact inputs): $L_\lambda(\theta)$ and atmospheric parameters $\tau_\lambda(\theta)$, $L_\lambda^\uparrow(\theta)$, and $L_\lambda^\downarrow(\theta)$ calculated using a given profile, surface type and viewing angle;

2. Imperfect atmosphere (i.e., inputs with errors): $L'_\lambda(\theta)$, $\tau'_\lambda(\theta)$, $L_\lambda^\uparrow(\theta)$, and $L_\lambda^\downarrow(\theta)$ calculated using perturbed temperature and humidity profiles to simulate real ‘imperfect’ input data (see next section for assumed errors used on the atmospheric profiles).

To further simulate the effects of instrument noise, the above two conditions were run by further adding random noise to the radiances based on a noise model that describes the sensor’s noise equivalent delta temperature (NEdT).

5.6 Error Propagation

The total LST uncertainty for the TES algorithm based on model, atmospheric and measurement noise contributions can be written as:

$$\delta LST_{TES} = [\delta LST_M + \delta LST_A + \delta LST_N]^{1/2} \quad (19)$$

where δLST_M is the model error due to assumptions made in the TES calibration curve, δLST_A is the atmospheric error, and δLST_N is the error associated with measurement noise. These errors are assumed to be independent.

To calculate the separate contributions from each of these errors let us first denote the simulated atmospheric parameters as $x = [\tau_\lambda(\theta), L_\lambda^\uparrow(\theta), L_\lambda^\downarrow(\theta)]$ and simulated observed radiance parameter as $y = L_\lambda(\theta)$. Both x and y are required to estimate the surface radiance that is input to the TES algorithm. In reality, however, the input parameters x are not known explicitly, but are associated with some error, δx , which we write as $\hat{x} = x + \delta x$. Similarly, the observed radiances have an associated noise based on the NEdT of the specific sensor, which we will denote by \hat{y} .

To characterize the retrieval (or model) error, we express the TES algorithm as a function based on perfect input parameters x and y such that $LST_{TES} = f(x, y)$. The model error, δLST_M , i.e.,

$$\delta LST_M = E[(f(x, y) - LST_{sim})^2 | x, y]^{1/2} \quad (20)$$

where LST_{sim} is the simulated LST used in the MODTRAN simulations, and $E[\cdot | x, y]$ denotes the mean-square error between the retrieved and simulated LST for inputs x and y .

In order to simulate an atmospheric error, the input atmospheric profiles were adjusted to simulate real data by applying random errors in the water vapor retrievals of between 10–20% that is typical for NWP models and retrieved water vapor estimates (Seemann et al. 2006). Accordingly, the relative humidity profiles were adjusted by scaling factors ranging from 0.8 to 1.2 (20%) in MODTRAN using a uniformly distributed random number generator. The atmospheric error can then be written as the difference between TES using perfect atmospheric inputs, x and imperfect inputs, \hat{x} :

$$\delta LST_A = E \left[(f(\hat{x}, y) - f(x, y))^2 | x, y \right]^{1/2} \quad (21)$$

And lastly the error due to measurement noise can be written as the difference between TES with perfect simulated TOA radiances, y and TES with noisy radiances, \hat{y} , assuming perfect atmospheric inputs, x :

$$\delta LST_N = E \left[(f(x, \hat{y}) - f(x, y))^2 | x, y \right]^{1/2} \quad (22)$$

Since the TES algorithm simultaneously retrieves the LST and spectral emissivity, the above equations also apply to the corresponding emissivity retrieval for each band.

To demonstrate the various error sources described above, Figure 15 shows results from a TEUSim run to quantify the relative contributions for three error sources including model (TES retrieval), instrument noise (NEdT = 0.2 K) and atmospheric (10% relative humidity error, and 1 K temperature error). A U.S. standard and a tropical atmospheric profile was used with the MODTRAN model. Results in Figure 15 show histograms of the total accuracy and precision

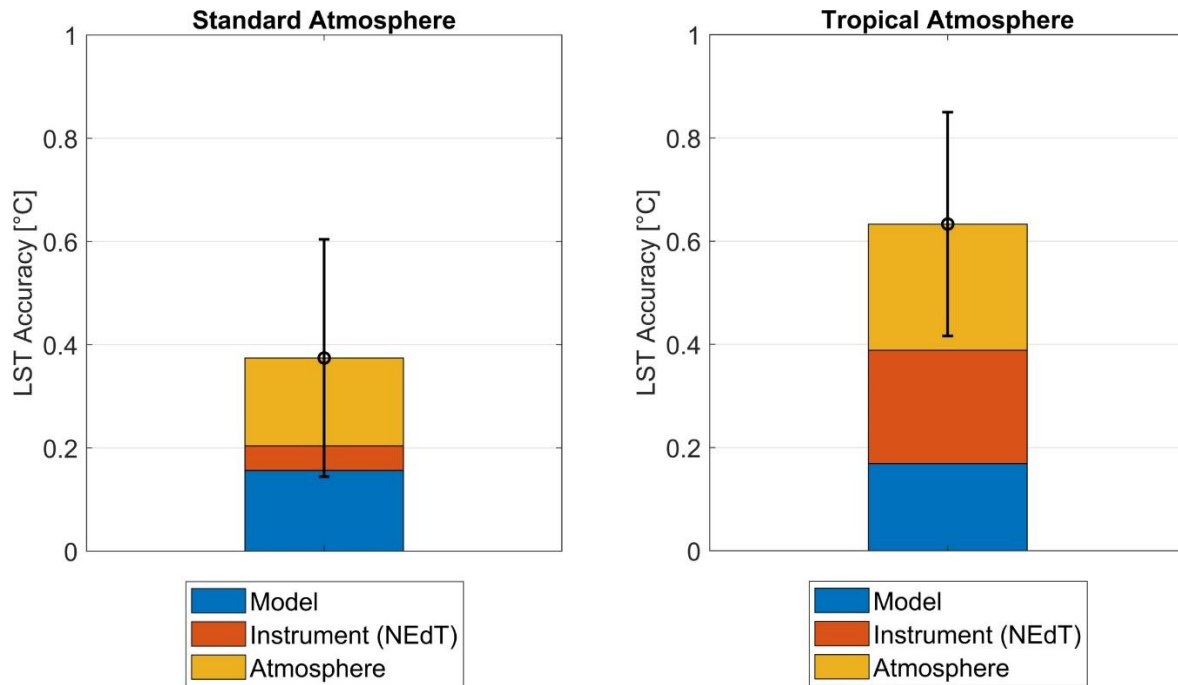


Figure 15. Histograms displaying the LST accuracy results of a 6-band TES approach with SBG TIR band locations for standard atmosphere (left) and tropical atmosphere (right), and for three different error sources including model (TES retrieval), instrument noise (NEdT = 0.2 K) and atmospheric (10% relative humidity error, and 1 K temperature error). 10,000 Monte Carlo simulations were run using MODTRAN and input ECOLib spectra of rocks, sands, soils, and vegetation. The errorbar represents the standard deviation (precision) of the simulation run for all errors combined.

(errobar) for the standard (nominal) and tropical (difficult case) atmospheres using 10,000 Monte Carlo simulations and input ECOLib spectra of rocks, sands, soils, and vegetation. The results show that for the standard atmosphere that the atmospheric correction error results in the largest error of 0.17 K, followed by the model error of 0.15 K and instrument noise had the smallest error of 0.05 K. For the tropical case, errors increase to 0.24 K for the atmospheric correction and to 0.22 K for the instrument noise, but the model error stays relatively stable with only slight increase to 0.17 K. This demonstrates that increasing the water vapor content has a large effect on both the atmospheric correction and instrument noise influence on the TES algorithm. The results are demonstrate that for SBG, the total accuracy of the L2 LST product is expected to be less than 1 K assuming that instrument noise is ≤ 0.2 K and input atmospheric

profiles are accurate to within 10% in relative humidity and 1 K in air temperature. These are typical error estimates of NWP models based on in situ validation results.

Table 6 shows uncertainty results using the SeeBor radiosounding database and four different surface classes including graybodies (vegetation, water, ice, snow), rocks, soils and sands all extracted from ECOLib. Random errors were simulated at each level using a uniformly distributed random number generator for the profiles (1 K temperature, 10% humidity, instrument noise of 0.2 K) and surface temperature estimated using equation 18. Two different versions of TES were used for the retrievals, a 3-band TES algorithm (SBG TIR bands 2, 5, 6) and a 5-band TES algorithm (SBG TIR bands 1, 2, 3, 5, 6). Simulations were all run at nadir view angle. The results show that rock samples had the greatest uncertainty in retrieved LST but was larger for the 3-band TES (1.45 K) when compared to the 5-band approach (1.2 K). This is due to larger scatter and uncertainty in the calibration curve when less bands are used for the regression, combined with the fact that rocks typically have larger spectral contrast and more difficult to retrieve spectral shapes. The total uncertainty for the 3-band approach was 1.15 K, while the 5-band approach had a total uncertainty below the 1 K level.

Table 6. LST total uncertainty expressed as the root mean square error (RMSE) using a 3-band and 5-band TES algorithm for 4 different surface classes with surface emissivity spectra from ECOLib (111 total samples), MODTRAN simulations, and SeeBor global radiosonde profiles. The LST uncertainty includes random errors in simulated air temperature (1 K), relative humidity profile (10%), and instrument noise (0.2 K) as discussed in the text.

Surface Type	Samples	Simulations	LST Total Uncertainty [K]	
			TES 3-band	TES 5-band
Vegetation, water, ice, snow	8	660,096	1.19	0.93
Rocks	48	3,960,686	1.45	1.16
Soils	45	3,713,040	0.90	0.81
Sands	10	825,120	0.99	0.92
Total	111	9,158,832	1.15	0.96

5.7 Parameterization of Uncertainties

A key requirement for generating a LST&E dataset is accurate knowledge of all contributing uncertainties. Uncertainties for each input product must be rigorously estimated for a variety of different conditions on a pixel-by-pixel basis before they can be merged and incorporated into a time series of measurements of sufficient length, consistency, and continuity to adequately meet the science requirements. The next logical step is to apply the uncertainty statistics produced from the TEUSim and apply them to estimate uncertainties from real data. To achieve this we use a simple empirical model where the total uncertainty, taken as the RMSE of the differences between simulated (truth) and retrieved LST&E, is regressed to the simulation inputs that showed the highest dependence error. These were the sensor view angle, total water vapor column amount, and land surface type. We then fit the total uncertainty with these independent variables using a least-squares method fit to a quadratic function. Three surface types were classified: graybody, transitional, and bare. The transitional surface represents a mixed cover type, and was calculated by varying the vegetation fraction cover percentage, f_v , by 25, 50, and 75% for the set of bare surface spectra (rocks, soils, sand) as follows:

$$\varepsilon_{trans} = \varepsilon_{gray} \cdot f_v + \varepsilon_{bare} \cdot (1 - f_v) \quad (23)$$

where ε_{trans} is the transition emissivity, ε_{gray} is a graybody emissivity spectrum (e.g., conifer), and ε_{bare} are the lab emissivities for bare surfaces.

The total uncertainty includes both a sensor view angle (SVA) and TCW dependence.

$$\begin{aligned} \delta LST_{SBG} = & a_0 + a_1 TCW + a_2 SVA + a_3 TCW \cdot SVA + a_4 TCW^2 \\ & + a_5 SVA^2 \end{aligned} \quad (24)$$

Similarly, the band-dependent emissivity uncertainties can be expressed as:

$$\delta \varepsilon_{i,SBG} = a_{i,0} + a_{i,1}TCW + a_{i,2}SVA + a_{i,3}TCW \cdot SVA + a_{i,4}TCW^2 + a_{i,5}SVA^2 \quad (25)$$

where δLST is the LST uncertainty (K) calculated as the difference between the simulated and retrieved LST, $\delta \varepsilon_i$ is the band-dependent emissivity uncertainty for band i , calculated as the difference between the input lab emissivity and retrieved emissivity, and a_i and $a_{i,j}$ are the LST and emissivity regression coefficients and depend on surface type (graybody, transition, bare).

A sensitivity study showed that the parameterizations given by equations 19–20 provided the best fit to the simulation results in terms of RMSE, with fits of ~ 0.1 K. Once the coefficients are established they can be applied on a pixel-by-pixel basis across any scene given estimates of TCW (usually extracted from the NWP data, e.g. GEOS5), and the SVA from the product metadata. A simple emissivity threshold using a band with large spectral variation can be used to

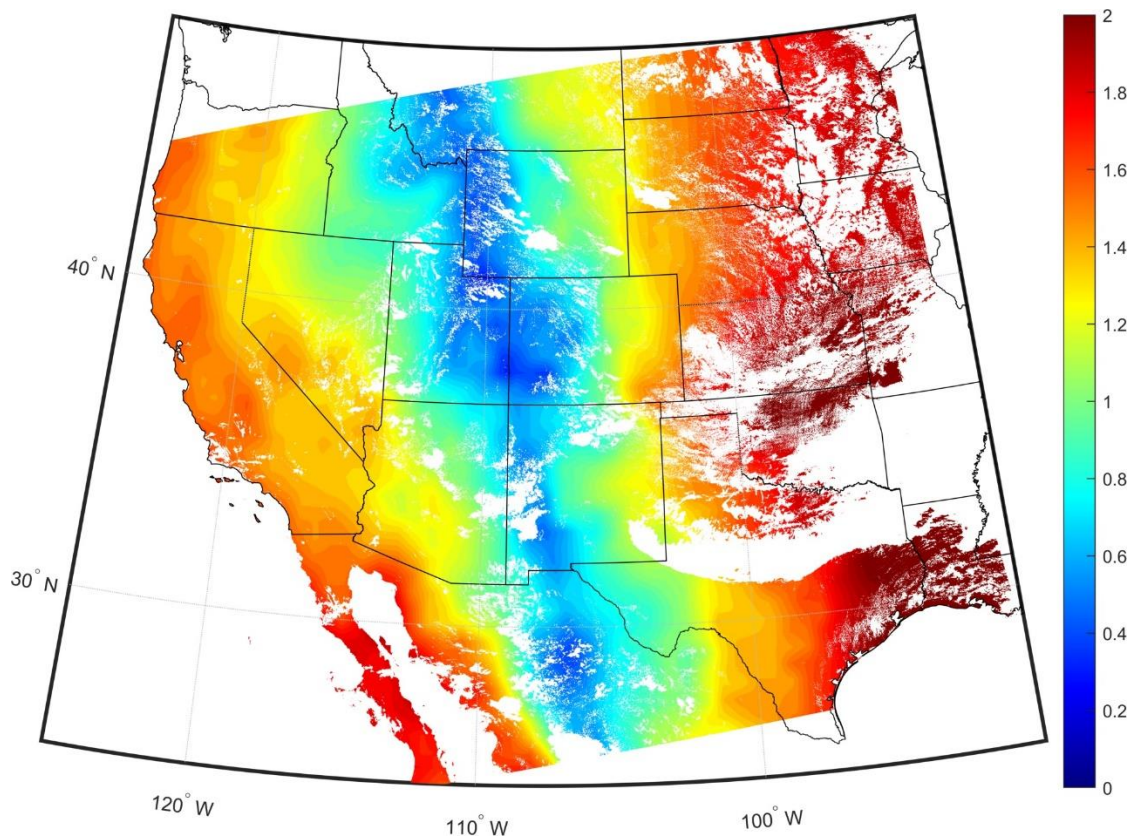


Figure 16. Example LST error for a VIIRS scene on 19 July 2023 over the western US using eq. 24. LST errors range from 0-2 and increase with higher PWV content and sensor view angle.

discriminate between graybody, transition, and bare types in any given scene for application of the relevant coefficients. This uncertainty model will be applied to SBG LST&E retrievals and included in the Scientific Data Set (SDS). The uncertainties will be calculated on a pixel-by-pixel basis for LST and emissivity for all 5 bands.

6 Emissivity anisotropy correction

LST data retrieved from TIR remote sensing can have strong directional dependencies due to the intrinsic heterogeneity of the land surface resulting in anisotropic emission. The directional behavior of the LST has been identified and quantified in numerous studies and is a major source of artificial variability/biases in LST data records (Duffour et al., 2016; Ermida et al., 2014; Guillevic et al., 2013; Rasmussen et al., 2011). Some of the LST variability with viewing angle can be attributed to emissivity, since most natural surfaces such as desert sands and forests are anisotropic emitters (Cao et al., 2019; Cuenca and Sobrino, 2004; García-Santos et al., 2012; Labed and Stoll, 1991; Lagouarde et al., 1995; Sobrino and Cuenca, 1999). The anisotropy of soil emissivity is related to geometrical effects of grain size, roughness and porosity (Labed and Stoll, 1991). A number of physical models (e.g. (Hapke, 1981; Moersch and Christensen, 1995; Pitman et al., 2005; Wald and Salisbury, 1995) and empirical models (e.g. (García-Santos et al., 2012; Nerry et al., 1991) have been used to address the angular dependence, however, since a sensor's field of view (FOV) may encompass a wide range of materials, it is difficult to translate laboratory or modeled emissivity anisotropy to the satellite pixel scale of tens of meters or more (Ermida et al. 2023). Therefore, Ermida et al. 2023 proposed a view angle dependent emissivity correction directly from the satellite pixel scale retrievals and applied to the TES algorithm.

The inputs to the TES algorithm (surface radiance, downwelling radiance) assume a Lambertian surface (isotropic), and the calibration curve uses a set of library emissivity spectra that have been measured in the lab with no angular dependence. As a result, Ermida et al. 2023 proposed a new methodology to derive the MMD calibration curve based on multi-sensor observations from a combination of Spinning Enhanced Visible and Infrared Imager (SEVIRI) on-board Meteosat Second Generation (MSG) satellites and the Visible Infrared Imaging Radiometer Suite (VIIRS) on-board the joint NASA/NOAA Suomi National Polar-orbiting Partnership (NPP). Taking advantage of the multi-angle view provided by the different sensors, Ermida et al. 2020 was able to characterize emissivity dependency of view zenith angle over a selection of sites over homogeneous desert regions. The correction was limited to bare areas since studies suggest that surface roughness introduced by vegetation tends to attenuate the anisotropy of emissivity (Sobrino et al., 2005).

6.1 MMD calibration curve with view angle dependence

Although the TES algorithm provides direct estimates of emissivity based on TOA satellite radiance measurements, (Ermida et al., 2020) showed that the TES can only accurately estimate angular effects of the channel IR8.7, since the MMD constrains the spectral variations of the emissivity with angle for the other channels. The work by Ermida et al. (2020) suggests that different MMD curves for different view angles might be necessary to account for emissivity anisotropy and proposed a reformulation of the MMD curve in order allow angular variations of the emissivity:

$$\varepsilon_{\min} = a_1 - a_2 MMD^{a'3} \quad (26)$$

with

$$a'_3 = a_3 + a_4 VZA^{a_5} \quad (27)$$

with the VZA with units of degrees. The calibration of the new MMD coefficients a_4 and a_5 cannot be obtained from spectral library data since these generally correspond to a nadir configuration. In order to obtain the needed data for the calibration, a multi-sensor retrieval approach was used at the selected sites. Because the spectral library is likely to provide coefficients with better accuracy, and the sites' retrievals are limited to desert bare ground conditions, only the a_4 and a_5 coefficients are fitted to the new data. To achieve that, equation (26) is first fitted to multi-sensor retrievals for different view zenith angle (VZA) classes, fixing a_1 and a_2 to the spectral library values, i.e. only coefficient a'_3 is fitted. Then, equation (27) is fitted to the previously obtained a'_3 values for each VZA class. Here, a_3 is also prescribed using the spectral library-based estimate and ultimately only a_4 and a_5 are fitted, yielding the values $a_4 = -5.6290 \times 10^{-7}$ and $a_5 = 2.7106$. Since the coefficients in equation (27) were derived from VIIRS TIR bands, they are valid for other sensors with a similar spectral range in TIR bands since the fit is based on the ϵ_{min} vs MMD curve. For this reason we will use the same coefficients derived from equation (27) for ECOSTRESS LST retrievals, which will have a very similar band configuration as SBG, and test the new SVA dependent calibration curve over selected sites with validation data (e.g. Gobabeb, Namibia). Since the maximum viewing angle with ECOSTRESS is 30 degrees (SBG will be 35 degrees) we expect the impact on LST&E retrievals to be relatively small, but non-negligible, especially over arid surfaces.

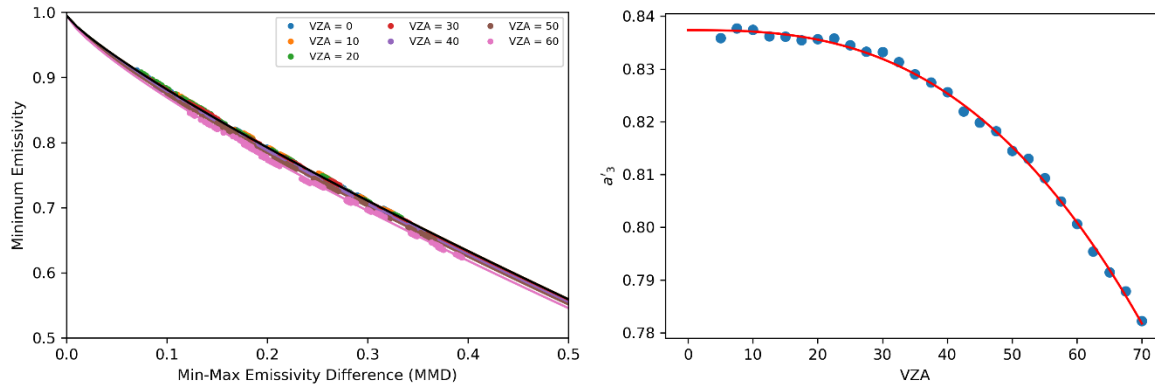


Figure 17 (left) MMD curves as obtained by fitting equation 26 to directional emissivity data derived with the multi-sensor method, for seven of the VZA bins; (right) Coefficient a'_3 of the MMD equation (eq. 26; blue) as function of the VZA and respective fitted curve (eq. 27; red).

7 Quality Control and Diagnostics

The T and ϵ products will need to be assessed using a set of quality control (QC) flags. These QC flags will involve automatic tests processed internally for each pixel and will depend on various retrieval conditions such as whether the pixel is over land or ocean surface, the atmospheric water vapor content (dry, moist, very humid, etc.), and cloud cover. The data quality attributes will be set automatically according to parameters set on data conditions during algorithm processing and will be assigned as either "bad," "suspect," or "good." Estimates of the accuracy and precision of the T and ϵ product will be reported in a separate data plane. At each step in the TES algorithm, various performance information will be output, which will give the user a summary of algorithm statistics in a spatial context. This type of information will be useful for determining surface type, atmospheric conditions, and overall performance of TES.

The architecture of the SBG data plane will be very similar to the ECOSTRESS T and ϵ QA data plane and the MOD21 product (Hulley et al. 2012a). It will consist of header information followed by an 8-bit QA data plane. The structure of the QA data plane will consist of ten primary fields, which are detailed in Table 7:

1. Mandatory QA flags: Overall description of status of pixel, produced with good quality, unreliable quality, not produced due to cloud, or other reasons than cloud.
2. Data Quality Field: good data, missing pixel, fairly and poorly calibrated are assigned to specific bit patterns.
3. Cloud Mask Field: Outputs from cloud mask statistics, e.g., optically thick or thin cloud, cirrus or contrails, clear, or snow/ice determined from NDSI threshold.
4. Cloud Adjacency: Clear pixels defined in the cloud mask will be assigned an adjacency category dependent on distance to the nearest cloud defined quantitatively by the number of pixels (e.g., very close, close, far, very far).
5. The final value of ϵ_{max} used in the NEM module after optimization (if necessary).
6. Number of iterations needed to remove reflected downwelling sky irradiance.
7. Atmospheric opacity test for humid scenes, using $L_{\lambda}^{\downarrow}/L'$ test.
8. MMD regime: $MMD < 0.3$ (near-graybody) or $MMD > 0.3$ (likely bare).
9. Emissivity accuracy (poor, marginal, good excellent).
10. LST accuracy (poor, marginal, good excellent).

The emissivity and LST accuracies described in bits 12-15 will be estimated from the uncertainty parameterization model. Classifying the performance level is based on typical validation results from using the TES algorithm from various instruments including ASTER and MODIS (Hulley and Hook 2011).

Pixels with 'unreliable quality' are typically either affected by nearby cloud, or have a large water vapor loading making the retrieval more uncertain. These pixels are flagged if they are within ~500 m of a detected nearby cloud, if the emissivity for the 12 micron is less than 0.95, or if the

transmissivity for that pixel is low (<0.3) due to a nearly opaque atmosphere (high water vapor). Emissivities for the 12 micron band usually invariant with respect to surface type and are high with values >0.96, unless the surface consists of rare mafic materials such as some basalts which are found in volcanic regions and have an unusually low emissivity in the longwave bands. If a pixel is affected by cloud, or there is incomplete atmospheric correction due to water vapor effects, band 5 emissivities will typically fall below 0.95.

Table 7. Bit flags defined in the QC SDS for the 5-band ECOSTRESS algorithm.

Bits	Long Name	Description
1&0	Mandatory QA flags	00 = Pixel produced, best quality 01 = Pixel produced, nominal quality. Either one or more of the following conditions are met: <ol style="list-style-type: none"> 1. emissivity in both 11 and 12 micron bands < 0.95, i.e. possible cloud contamination 2. low transmissivity due to high water vapor loading (<0.4), check PWV values and error estimates 10 = Pixel produced, but cloud detected 11 = Pixel not produced due to missing/bad data, user should check Data quality flag bits
3 & 2	Data quality flag	00 = Good quality L1B data 01 = not set 10 = not set 11 = Missing/bad L1B data
5 & 4	Cloud/Ocean Flag	tbd
7 & 6	Iterations	00 = Slow convergence 01 = Nominal 10 = Nominal

		11 = Fast
9 & 8	Atmospheric Opacity	00 = ≥ 3 (Warm, humid air; or cold land) 01 = 0.2 - 0.3 (Nominal value) 10 = 0.1 - 0.2 (Nominal value) 11 = < 0.1 (Dry, or high altitude pixel)
11 & 10	MMD	00 = > 0.15 (Most silicate rocks) 01 = 0.1 - 0.15 (Rocks, sand, some soils) 10 = 0.03 - 0.1 (Mostly soils, mixed pixel) 11 = < 0.03 (Vegetation, snow, water, ice)
13 & 12	Emissivity accuracy	00 = > 0.02 (Poor performance) 01 = 0.015 - 0.02 (Marginal performance) 10 = 0.01 - 0.015 (Good performance) 11 = < 0.01 (Excellent performance)
15 & 14	LST accuracy	00 = > 2 K (Poor performance) 01 = 1.5 - 2 K (Marginal performance) 10 = 1 - 1.5 K (Good performance) 11 = < 1 K (Excellent performance)

8 Scientific Data Set (SDS) Variables

The SBG LST&E products will be archived in Hierarchical Data Format 5 - Earth Observing System (HDF5-EOS) format files. HDF is the standard archive format for NASA EOS Data Information System (EOSDIS) products. The LST&E product files will contain global attributes described in the metadata, and scientific data sets (SDSs) with local attributes. Unique in HDF-EOS data files is the use of HDF features to create point, swath, and grid structures to support geolocation of data. These structures (Vgroups and Vdata) provide geolocation relationships between data in an SDS and geographic coordinates (latitude and longitude or map projections) to support mapping the data. Attributes (metadata), global and local, provide various information about the data. Users unfamiliar with HDF and HDF-EOS formats may wish to consult Web sites listed in the Related Web Sites section for more information.

The scientific variable arrays that will be output in the SBG L2 product are highlighted in Table 8, including descriptions of data type, units, valid range, fill value, scale factor and offset. The sequence begins as a swath (scene) at a nominal pixel spatial resolution of 60x60 meters at nadir and a nominal swath width of 935 km. The data types and scaling factors have been optimized to minimize the amount of memory required to store the data.

Table 8. The Scientific Data Sets (SDSs) for the ECOSTRESS L2 product.

SDS	Long Name	Data type	Units	Valid Range	Fill Value	Scale Factor	Offset
Group	SDS (per pixel, 5400 * 5632)						
LST	Land Surface Temperature	uint16	K	7500-65535	0	0.02	0.0
QC	Quality control for LST and emissivity	uint16	n/a	0-65535	n/a	n/a	n/a
Emis1	Band 1 emissivity	uint8	n/a	1-255	0	0.002	0.49
Emis2	Band 2 emissivity	uint8	n/a	1-255	0	0.002	0.49
Emis3	Band 3 emissivity	uint8	n/a	1-255	0	0.002	0.49
Emis4	Band 4 emissivity	uint8	n/a	1-255	0	0.002	0.49
Emis5	Band 5 emissivity	uint8	n/a	1-255	0	0.002	0.49
Emis6	Band 6 emissivity	uint8	n/a	1-255	0	0.002	0.49
Emis7	Band 7 emissivity	uint8	n/a	1-255	0	0.002	0.49
Emis8	Band 8 emissivity	uint8	n/a	1-255	0	0.002	0.49
LST_Err	Land Surface Temperature error	uint8	K	1-255	0	0.04	0.0
Emis1_Err	Band 1 emissivity error	uint16	n/a	0-65535	0	0.0001	0.0
Emis2_Err	Band 2 emissivity error	uint16	n/a	0-65535	0	0.0001	0.0
Emis3_Err	Band 3 emissivity error	uint16	n/a	0-65535	0	0.0001	0.0
Emis4_Err	Band 4 emissivity error	uint16	n/a	0-65535	0	0.0001	0.0
Emis5_Err	Band 5 emissivity error	uint16	n/a	0-65535	0	0.0001	0.0
Emis6_Err	Band 6 emissivity error	uint16	n/a	0-65535	0	0.0001	0.0
Emis7_Err	Band 7 emissivity error	uint16	n/a	0-65535	0	0.0001	0.0
Emis8_Err	Band 8 emissivity error	uint16	n/a	0-65535	0	0.0001	0.0
EmisWB	Wideband emissivity	uint8	n/a	1-255	0	0.002	0.49
PWV	Precipitable Water Vapor	uint16	cm	0-65535	n/a	0.001	0.0
water_mask	Land/water mask	uint8	1=water	0-1	255	1	0

			0=land				
cloud_mask	Land/water mask	uint8	1=cloud 0=clear	0-1	255	1	0
height	Ground elevation	int16	meters	-1000- 10000	-32768	1	0
Range	Satellite to pixel range	int16	meters	0-32767	-32768	100	800000
view_zenith	Sensor zenith angle	int16	degrees	0-18000	-32768	0.01	0.0

9 Calibration/Validation Plans

The SBG payload will have two blackbodies operating at approximately 300 K and 340 K. Both blackbodies will be viewed with each cross-track sweep every 1.29 seconds to provide gain and offset calibrations. During pre-flight ground calibration, a large high-emissivity cavity blackbody target will be measured to provide radiometric calibration. Data from the ground calibration will be used to correct the expected small errors intrinsic to compact flight blackbodies, and any radiometer nonlinearity. All flight and ground calibration blackbodies will utilize redundant NIST-traceable temperature sensors. The calibrated TIR data will have a 300 K radiometric accuracy of 0.5 K and a radiometric precision of 0.1 K in 6 spectral bands.

In addition to calibration with blackbodies, SBG will perform vicarious calibration using a well characterized set of ground calibration/validation sites shown in Table 10. Calibration/Validation sites will include well established water, vegetation, and barren targets (Hook et al. 2004; Hulley et al. 2009a). Many of these sites are currently being used to validate the TIR measurements of ASTER, MODIS and ECOSTRESS LST data (Hook et al. 2007; Hulley et al. 2022; Hulley et al. 2009a). This work will be conducted as part of the SDS activities and will ensure that the ECOSTRESS data and products meet the required accuracy, precision and uncertainty.

Two methods have been established for validating LST data: a conventional T-based method and an R-based method (Wan and Li 2008). The T-based method requires ground measurements over thermally homogenous sites concurrent with the satellite overpass, while the R-based method relies on a radiative closure simulation in a clear atmospheric window region to

Table 9. ECOSTRESS targets include all of CONUS plus 1,000 km regions centered on climate hotspots, agricultural regions, and FLUXNET validation sites. ENF: evergreen needleleaf forest; EBF: evergreen broadleaf forest; WSA: woody savanna; SAV: Savanna; CRO: cropland; DBF: Deciduous Broadleaf Forest; Cal/Val: LST Calibration/Validation.

Site	Biome Type	Latitude	Longitude
Climate Hotspot Regions			
Boreal North America	ENF	47.0	-87.0
Boreal Eurasia	ENF	47.0	45.0
Tropical/Dry Transition 1	EBF	-12.0	-67.0
Tropical/Dry Transition 2	EBF/WSA	-16.0	-50.0
Tropical/Dry Transition 3	EBF/WSA	20.0	-103.0
Tropical/Dry Transition 4	WSA/SAV	9.0	4.0
Tropical/Dry Transition 5	WSA/SAV	-23.0	22.0
Agricultural Regions			
Agricultural North America 1	CRO	35.7	-121.0
Agricultural North America 2	CRO	41.5	-98.7
Agricultural Eurasia 1	CRO	44.2	18.0
Agricultural Eurasia 2	CRO	25.0	78.0
Agricultural Eurasia 3	CRO	47.0	0.0
ET and LST Validation Sites			
Campbell River, Canada	ENF	49.9	-125.3
Hartheim, Germany	ENF	47.9	7.6
Howland Forest, ME, USA	ENF	45.2	-68.7
Metolius, OR, USA	ENF	44.5	-121.6
Quebec Boreal, Canada	ENF	49.7	-74.3
Tatra, Slovak Republic	ENF	49.1	20.2
Wind River Crane, WA, USA	ENF	45.8	-122.0
Guyaflex, French Guyana	EBF	5.3	-52.9
La Selva, Costa Rica	EBF	10.4	-84.0
Manaus K34, Brazil	EBF	-2.6	-60.2
Santarem KM67, Brazil	EBF	-2.9	-55.0
Santarem KM83, Brazil	EBF	-3.0	-55.0
Chamela, Mexico	DBF	19.5	-105.0
Duke Forest, NC, USA	DBF	36.0	-79.1
Hainich, Germany	DBF, Cal/Val	51.1	10.5
Harvard Forest, MA, USA	DBF	42.5	-72.2
Hesse Forest, France	DBF	48.7	7.1
Tonzi Ranch, CA, USA	DBF/WSA	38.4	-121.1
ARM S. Great Plains, OK, USA	CRO	36.6	-97.5
Aurade, France	CRO	43.5	1.1
Bondville, IL, USA	CRO, Cal/Val	40.0	-88.3
El Saler-Sueca, Spain	CRO	39.3	-0.3
Mead 1, 2, 3 NE, USA	CRO	41.2	-96.5
Salton Sea, CA	Cal/Val	33.3	-115.7
Lake Tahoe, CA	Cal/Val	39.15	-120
Gobabeb, Namibia	Cal/Val	23.55	15.05
Algodones Dunes, CA	Cal/Val	33.0	-115.1

estimate the LST from top of atmosphere (TOA) observed brightness temperatures, assuming the emissivity is known from ground measurements. The T-based method is the preferred method, but it requires accurate in-situ measurements that are only available from a small number of thermally homogeneous sites concurrently with the satellite overpass. The R-based method is not a true validation in the classical sense, but it is useful for exposing biases in LST products and doesn't require simultaneous in-situ measurements and is therefore easier to implement both day and night over a larger number of global sites; however, it is susceptible to errors in the atmospheric correction and emissivity uncertainties.

Emissivity samples have been collected at the Algodones and Gobabeb Cal/Val sites and their emissivity determined in the laboratory using a Nicolet 520 FT-IR spectrometer (Gottsche and Hulley 2012b). Validation of emissivity data from space ideally requires a site that is homogeneous in emissivity at the scale of the imagery, allowing several image pixels to be validated over the target site. A validation study at the Land Surface Analysis–Satellite Application Facility (LSA-SAF) Gobabeb validation site in Namibia showed that MODIS emissivities derived from a 3-band TES approach (MOD21 product) matched closely with in-situ emissivity data (~1%), while emissivities based on land cover classification products (e.g., SEVIRI, MOD11) overestimated emissivities over the sand dunes by as much as 3.5% (Gottsche and Hulley 2012a). Similar studies will be performed with ECOSTRESS to determine if the spectral shapes of the emissivity retrievals are consistent with in situ measurements.

We plan to use the Lake Tahoe and Salton Sea automated validation sites for cal/val over water bodies. At these sites measurements of skin temperature have been made every two minutes since 1999 (Tahoe) and 2006 (Salton Sea) and are used to validate the mid and thermal infrared data and products from ASTER and MODIS (Hook et al. 2007). Water targets are ideal

for cal/val activities because they are thermally homogeneous and the emissivity is generally well known. A further advantage of Tahoe is that the lake is located at high altitude, which minimizes atmospheric correction errors, and is large enough to validate sensors from pixel ranges of tens of meters to several kilometers. Figure 18 shows an example of differences between the standard MODIS (MOD11_L2) and ASTER (AST08) LST products and in-situ measurements at Lake Tahoe. The MODIS product is accurate to ± 0.2 K, while the ASTER product has a bias of 1 K due to residual atmospheric correction effects. The typical range of temperatures at Tahoe is from 5°C to 25°C. More recently in 2008, an additional cal/val site at the Salton Sea was established. Salton Sea is a low-altitude site with significantly warmer temperatures than Lake Tahoe (up to 35°C), and together they provide a wide range of different conditions.

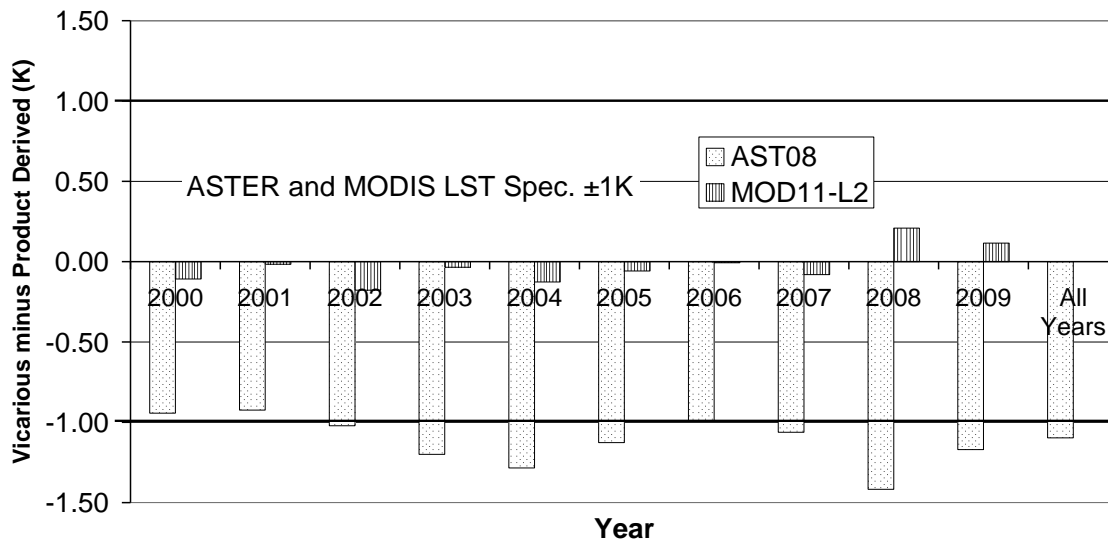


Figure 18. Difference between the MODIS (MOD11_L2) and ASTER (AST08) LST products and in-situ measurements at Lake Tahoe. The MODIS product is accurate to ± 0.2 K, while the ASTER product has a bias of 1 K due to residual atmospheric correction effects since the standard product does not use a Water Vapor Scaling (WVS) optimization model.

For vegetated surface types we will use a combination of data from the Surface Radiation Budget Network (SURFRAD) and FLUXNET sites. For SURFRAD, we will use a set of six sites established in 1993 for the continuous, long-term measurements of the surface radiation budget over the United States through the support of NOAA's Office of Global Programs (<http://www.srrb.noaa.gov/surfrad/>). The six sites (Bondville, IL; Boulder, CO; Fort Peck, MT; Goodwin Creek, MS; Penn State, PA; and Sioux Falls, SD) are situated in large, flat agricultural areas consisting of crops and grasslands and have previously been used to assess the MODIS and ASTER LST&E products with some success (Augustine et al. 2000; Wang and Liang 2009). From FLUXNET and the Carbon Europe Integrated Project (<http://www.carboeurope.org/>), we will include an additional four sites to cover the broadleaf and needleleaf forest biomes (e.g., Hainich and Hartheim, Germany; Hesse Forest and Aurade, France; El Saler-Sueca, Spain), using data from the FLUXNET as well as data from the EOS Land Validation Core sites (http://landval.gsfc.nasa.gov/coresite_gen.html). We will further use data from the Atmospheric Radiation Measurement (ARM) cal/val site in Oklahoma, USA for validation of LST. The Southern Great Plains (SGP) site was the first field measurement site established by DOE's ARM Program. The SGP site consists of in situ and remote-sensing instrument clusters arrayed across approximately 55,000 square miles (143,000 square kilometers) in north-central Oklahoma.

For LST validation over arid regions, we will use two pseudo-invariant, homogeneous sand dune sites located in southwestern USA (Algodones dunes) and in Namibia (Gobabeb). These sites have already been used for validating ASTER, MODIS, and AIRS LST products, (Hulley et al. 2009b). The emissivity and mineralogy of samples collected at these sites have been well characterized and are described by Hulley et al. (2009a).

Pseudo-invariant ground sites such as playas, salt flats, and claypans have been increasingly recognized as optimal targets for the long-term validation and calibration of visible, shortwave, and thermal infrared data (Bannari et al. 2005; Cosnefroy et al. 1996; de Vries et al. 2007; Teillet et al. 1998). We have found that large sand dune fields are particularly useful for the validation of TIR emissivity data (Hulley and Hook 2009a). Sand dunes have consistent and homogeneous mineralogy and physical properties over long time periods. They do not collect water for long periods as playas and pans might, and drying of the surface does not lead to cracks and fissures, typical in any site with a large clay component, which could raise the emissivity due to cavity radiation effects (Mushkin and Gillespie 2005). Furthermore, the mineralogy and composition of sand samples collected in the field can be accurately determined in the laboratory using reflectance and x-ray diffraction (XRD) measurements. In general, the dune sites should be spatially uniform and any temporal variability due to changes in soil moisture and vegetation cover should be minimal. Ideally, the surface should always be dry, since any water on the surface can increase the emissivity by up to 0.16 (16%) in the 8.2–9.2- μm range depending on the type of soil (Mira et al. 2007).

9.1 Emissivity Validation Methodology

Seasonal changes in vegetation cover, aeolian processes such as wind erosion, deposition and transport, and daily variations in surface soil moisture from precipitation, dew, and snowmelt are the primary factors that could potentially affect the temporal stability and spatial uniformity of the pseudo-invariant sand dune cal/val sites. The presence of soil moisture would result in a significant increase in TIR emissivity at the dune sites, caused by the water film on the sand particles decreasing its reflectivity (Mira et al. 2007; Ogawa et al. 2006), particularly for MODIS

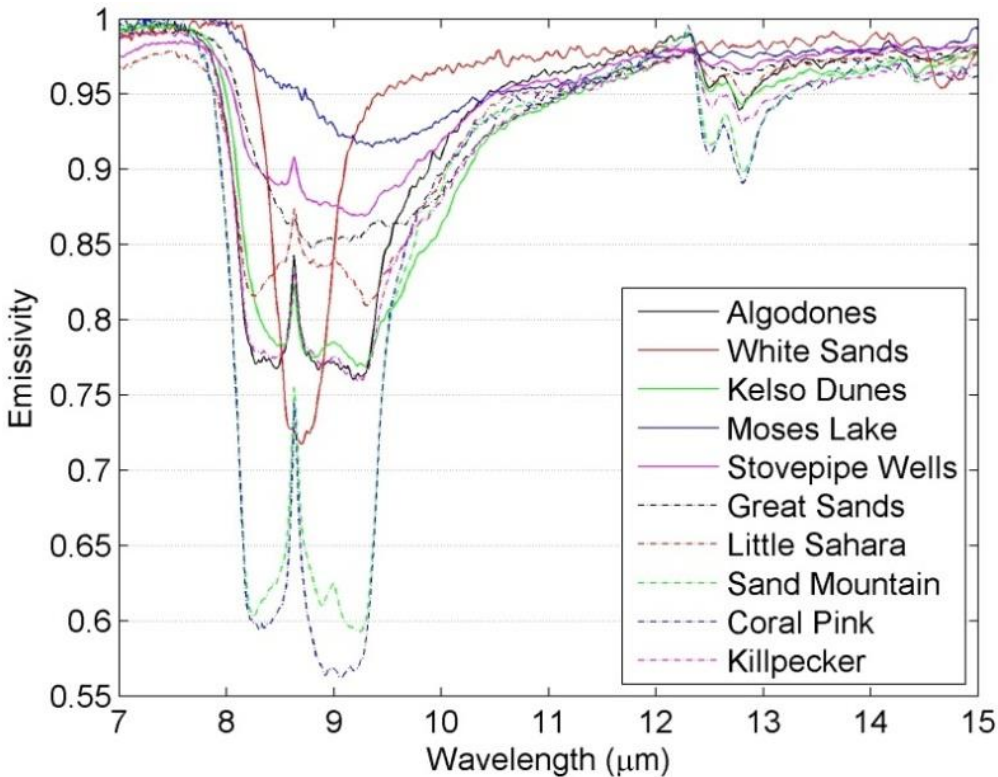


Figure 19. Laboratory-measured emissivity spectra of sand samples collected at ten pseudo-invariant sand dune validation sites in the southwestern United States. The sites cover a wide range of emissivities in the TIR region.

band 29 in the quartz Reststrahlen band. However, given that the dune validation sites are aeolian (high winds), at high altitude (low humidity), and in semi-arid regions (high skin temperatures), the lifetime of soil moisture in the first few micrometers of the surface skin layer as measured in the TIR is most likely small due to large sensible heat fluxes and, therefore, high evaporation rates, in addition to rapid infiltration. Consequently, we hypothesize that it would most likely take a very recent precipitation event to have any noticeable effect on remote-sensing observations of TIR emissivity over these types of areas.

Figure 19 shows emissivity spectra from sand dune samples collected at ten sand dune sites in the southwestern United States. The spectra cover a wide range of emissivities in the TIR region. These sites will be the core sites used to validate the emissivity and LST products from

ECOSTRESS. Figure 20 shows ASTER false-color visible images of each dune site and comparisons between the retrieved ASTER emissivity spectra and lab measurements. The lab spectra in Figure 20 show the mean and standard deviation (spatial) in emissivity for all sand samples collected at the site, while the ASTER spectra give the mean emissivity and combined spatial and temporal standard deviation for all observations acquired during the summer (July–September) time periods. The results show that a 5-band TES derived emissivity from ASTER data captures the spectral shape of all the dune sands very well. The quartz doublet centered around ASTER band 11 (8.6 μm) is clearly visible for Algodones Dunes samples, and the characteristic gypsum minimum in ASTER band 11 (8.6 μm) is evident from the White Sands samples. Similar results are expected for the 5-band TES algorithm planned for ECOSTRESS

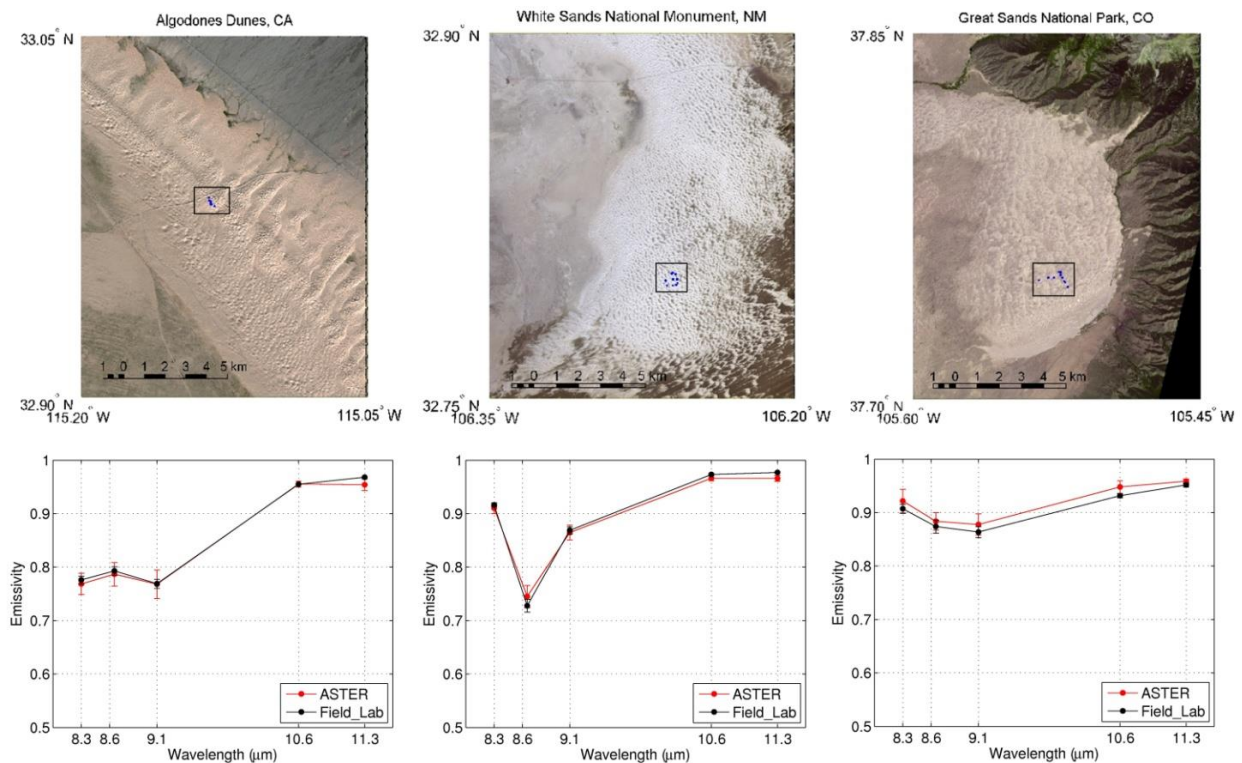


Figure 20. ASTER false-color visible images (top) and emissivity spectra comparisons between ASTER TES and lab results for Algodones Dunes, California; White Sands, New Mexico; and Great Sands, Colorado (bottom). Squares with blue dots indicate the sampling areas. ASTER error bars show temporal and spatial variation, whereas lab spectra show spatial variation.

9.2 LST Validation Methodology

9.2.1 Radiance-based Approach

For LST validation over the sand dune sites, we will use a recently established R-based validation method (Coll et al. 2009b; Wan and Li 2008). The advantage of this method is that it does not require in-situ measurements, but instead relies on atmospheric profiles of temperature and water vapor over the site and an accurate estimation of the emissivity. The R-based method is based on a ‘radiative closure simulation’ with input surface emissivity spectra from either lab or field measurements, atmospheric profiles from an external source (e.g., model or radiosonde), and the retrieved LST product as input. A radiative transfer model is used to forward model these parameters to simulate at-sensor BTs in a clear window region of the atmosphere (11–12 μm). The input LST product is then adjusted in 2-K steps until two calculated at-sensor BTs bracket the observed BT value. An estimate of the ‘true’ temperature ($LST_{R-based}$) is then found by interpolation between the two calculated BTs, the observed BT, and the initial retrieved LST used in the simulation. The LST error, or uncertainty in the LST retrieval is simply found by taking the difference between the retrieved LST product and the estimate of $LST_{R-based}$. This method has been successfully applied to MODIS LST products in previous studies (Coll et al. 2009a; Wan and Li 2008; Wan 2008). For MODIS data, band 31 (10.78–11.28 μm) is typically used for the simulation since it is the least sensitive to atmospheric absorption in the longwave region. The advantage of the R-based method is that it can be applied to a large number of global sites where the emissivity is known (e.g., from field measurements) and during night- and daytime observations to define the diurnal temperature range.

Wan and Li (2008) proposed a quality check to assess the suitability of the atmospheric profiles by looking at differences between observed and calculated BTs in two nearby window

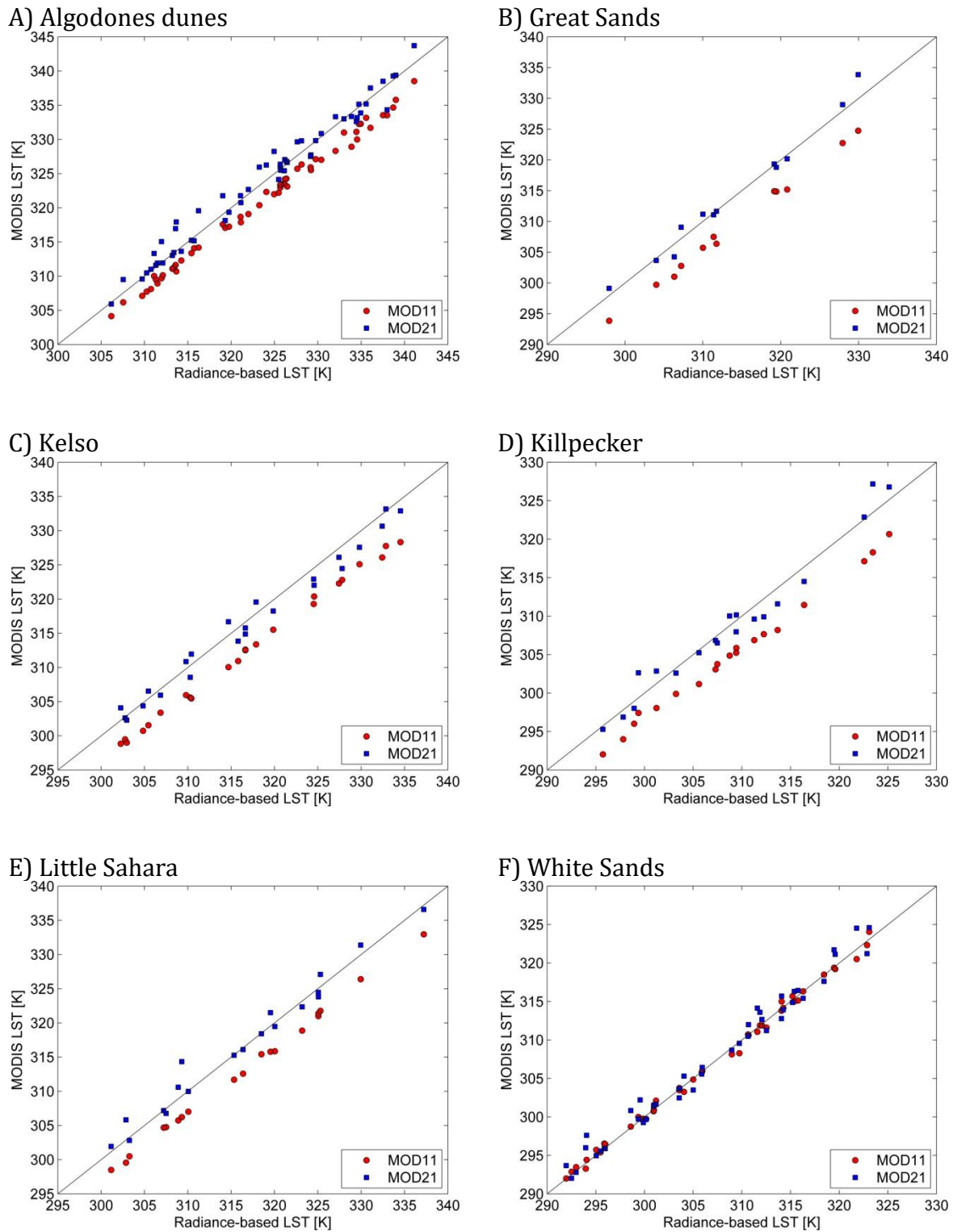


Figure 21. An example of the R-based validation method applied to the MODIS Aqua MOD11 and MOD21 LST products over six pseudo-invariant sand dune sites using all data during 2005. AIRS profiles and lab-measured emissivities from samples collected at the sites were used for the R-based calculations.

regions with different absorption features. For example, the quality check for MODIS bands 31 and 32 at 11 and 12 μm is:

$$\delta(T_{11} - T_{12}) = (T_{11}^{obs} - T_{12}^{obs}) - (T_{11}^{calc} - T_{12}^{calc}) \quad (1)$$

where: T_{11}^{obs} and T_{12}^{obs} are the observed brightness temperatures at 11 and 12 μm respectively, and T_{11}^{calc} and T_{12}^{calc} are the calculated brightness temperatures from the R-based simulation at 11 and 12 μm respectively. If $\delta(T_{11} - T_{12})$ is close to zero, then the assumption is that the atmospheric temperature and water vapor profiles are accurately representing the true atmospheric conditions at the time of the observation, granted the emissivity is already well known. Because water vapor absorption is higher in the 12- μm region, negative residual values of $\delta(T_{11} - T_{12})$ imply the R-based profiles are overestimating the atmospheric effect, while positive values imply an underestimation of atmospheric effects. A simple threshold can be applied to filter out any unsuitable candidate profiles for validation. Although Wan and Li (2008) proposed a threshold of ± 0.3 K for MODIS data, we performed a sensitivity analysis and found that a threshold of ± 0.5 K resulted in a good balance between the numbers of profiles accepted and accuracy of the final R-based LST. Figure 21 shows an example of the R-based validation method applied to the MODIS Aqua MOD11 and MOD21 LST products over six pseudo-invariant sand dune sites using all data during 2005. AIRS profiles and lab-measured emissivities from samples collected at the sites were used for the R-based calculations. The results show that the MOD11 SW LST algorithm underestimates the LST by 3–4 K at all sites except White Sands, while the MOD21 algorithm has biases of less than 0.5 K. The statistics of the results including bias and RMSE are shown in Table 13. MOD11 RMSEs are as high as ~ 5 K at Great Sands, while MOD21 RMSEs are mostly at the 1.6 K level. The reason for the MOD11 cold bias is that the emissivity for barren surfaces is assigned one value that is fixed (~ 0.96 at 11 μm). This

causes large LST errors over bare sites where the mineralogy results in emissivities lower than that fixed value. The MOD21 algorithm, on the other hand, physically retrieves the spectral emissivity in MODIS bands 29, 31, and 32, along with the LST, and this results in more accurate LST results, particularly over bare regions where emissivity variations can be large, both spatially and spectrally. Table 14 shows comparisons between the laboratory-derived emissivities at each site, along with the mean MOD11 and MOD21 emissivities for band 31 (11 μm).

9.2.1.1 Uncertainty Analysis of R-based approach

The uncertainty in the R-based LST estimate ($LST_{R-based}$) was calculated by perturbing the atmospheric temperature and water vapor profiles, and by varying the surface emissivity. Atmospheric effects were simulated by first increasing the relative humidity at each NCEP level by 10%, and then by increasing the air temperature by 1 K at each level. The effect on the accuracy of $LST_{R-based}$ was estimated as the calculated LST difference between the original and the perturbed profiles for the 11 μm window region. The results are summarized in Table 11. Using a standard profile with total column water vapor of 2 cm, the absolute LST differences were 0.35 K for the water vapor variation (10%), and 0.19 K for the air temperature variation (1 K), resulting in a total atmospheric effect of ± 0.39 K. Using an emissivity perturbation of 0.005 (0.5%), which represents the maximum spatial variation found from the lab measured spectra and ASTER data at each site, resulted in an absolute LST difference of 0.23 K. Validation of the Stand-Alone AIRS Radiative Transfer Algorithm (SARTA) with in situ data have shown accuracies approaching 0.2 K depending on the wavenumber region (Strow et al. 2006), and this uncertainty was considered negligible. The total combined root mean square error (RMSE) for the uncertainty in $LST_{R-based}$ based on estimated atmospheric profile, emissivity and radiative

transfer model errors was ± 0.47 K. This is within the 1 K accuracy requirement for typical in situ measurements of LST (Hook et al. 2007).

Further, since air temperature and water vapor errors (and emissivity) typically cancel each other out and may have different signs at different levels, the simulated error of 0.47 K is most likely an overestimate, i.e. a 'worse-case-scenario'. Also, using the brightness temperature profile quality check would most likely filter out the majority of unsuitable profiles.

Table 10. Uncertainty analysis results showing how perturbations in emissivity, air temperature and relative humidity affect the relative accuracy of the R-based LST derivation.

Parameter	Perturbation	R-based LST Change
Emissivity	$\epsilon + 0.005$	0.23 K
Air Temperature	$T_{air} + 1 K$	0.19 K
Relative Humidity	RH + 10%	0.35 K

Table 11. R-based LST validation statistics from six pseudo-invariant sand dune sites using all MOD11 and MOD21 LST retrievals during 2005.

	MOD11 Bias	MOD11 RMSE	MOD21 Bias	MOD21 RMSE
Algodones (197 scenes)	-2.65	2.78	0.50	1.60
Great Sands (123 Scenes)	-4.71	4.74	0.43	1.52
Kelso (210 scenes)	-4.52	4.58	-0.67	1.64
Killpecker (147 scenes)	-4.07	4.16	-0.09	1.68
Little Sahara (159 scenes)	-3.42	3.47	0.52	1.63
White Sands (102 scenes)	-0.06	0.54	0.48	1.34

Table 12. Emissivity comparisons between lab, MOD11, and MOD21 at six pseudo-invariant sand sites.

	Lab	MOD11	MOD21
Algodones (197 scenes)	0.963	0.966	0.954
Great Sands (123 Scenes)	0.944	0.970	0.949
Kelso (210 scenes)	0.942	0.966	0.949
Killpecker (147 scenes)	0.942	0.968	0.946
Little Sahara (159 scenes)	0.953	0.972	0.952
White Sands (102 scenes)	0.976	0.974	0.967

9.2.2 Temperature-based (T-based) LST Validation Method

The T-based method provides the best evaluation of the ability for a LST retrieval algorithm to invert the satellite radiometric measurement and accurately account for emissivity and atmospheric effects. The difficulty of this method over land is that several accurate, well calibrated ground radiometers are required to make rigorous measurements concurrently with the satellite overpass over a large thermally homogeneous area ideally representing several pixels at the remote sensing scale. Field radiometers typically measure the radiometric temperature of the surface being measured, and this measurement has to be corrected for the reflected downwelling radiation from the atmosphere and the emissivity before the surface skin temperature can be obtained. An example of two state-of-the-art T-based validation sites are discussed next, Lake Tahoe, CA/NV and Salton Sea, CA.

Lake Tahoe is large clear freshwater lake situated on the California/Nevada border at 1,996 m elevation making it the largest Alpine lake in North America, and USA's second deepest. The Lake Tahoe automated calibration/validation site, was established in 1999 with four buoys, referred to as TB1, TB2, TB3 and TB4, which provide simultaneous measurements of skin and bulk temperatures in addition to meteorological data (air temperature, relative humidity,

wind speed and direction) every two minutes (Hook et al. 2007). Each buoy includes a custom-built radiometer developed by JPL that has accuracies below the 0.1 K level. Calibration results have shown good agreement with other well-calibrated radiometers to within ± 0.05 K (Barton et al. 2004). The radiometric measurements are converted to skin temperatures by accounting for the effects of emissivity and reflected downwelling sky radiation. For emissivity, an emissivity spectrum of water from the ASTER spectral library is used (<http://speclib.jpl.nasa.gov>) (Baldrige et al. 2009), and the reflected downwelling irradiance is computed using radiative transfer simulations with atmospheric profiles input from NCEP data (Hook et al. 2003). Figure 22 shows an example of the T-based validation results for ECOSTRESS LST versus in situ LST measurements for all T-based sites at Lake Constance, Gobabeb, Lake Tahoe, Salton Sea and Russell ranch.

The Salton Sea validation site is situated on a platform located in the southwest corner of the lake and was established more recently at the end of 2007. In contrast to Lake Tahoe, the Salton Sea is a large saline lake situated in southeastern California at an elevation of 75 m below sea-level. In situ measurements at these two lakes provide the most comprehensive and largest data record of water skin temperatures available. The high quality and frequency of the measurements over long time periods and for a wide range of surface temperatures (~ 4 to 35 °C) and atmospheric conditions make this an excellent in situ dataset for validation and calibration of multiple sensors with different overpass times (Hook et al. 2004; Hook et al. 2003; Hook et al. 2007; Tonooka et al. 2005).

The T-based method becomes increasingly more difficult for sensor's with coarser spatial resolutions (e.g. MODIS 1km) over land where surface emissivities become spatially and spectrally more variable. For example, at the ASTER pixel scale (90 m), depending on the

homogeneity of the surface, several radiometer measurements are required over the land surface being measured to account for LST variability which could vary by as much as 10 K over a few meters (Coll et al. 2009a). Point measurements from flux towers or radiometer measurements exist but are not fully representative of the surrounding surface variability at coarse spatial scales. Researchers are investigating upscaling techniques from in situ to satellite LST measurements, for example by using the Soil Moisture Monitoring - land surface model (SETHYS) (Coudert et al. 2006; Guillevic et al. 2012). However, the fact remains that validating satellite LST data at >1km scale with in situ data over land remains a big challenge due to surface temperature variability that depends on many factors including season, time of day, surface type and meteorological conditions.

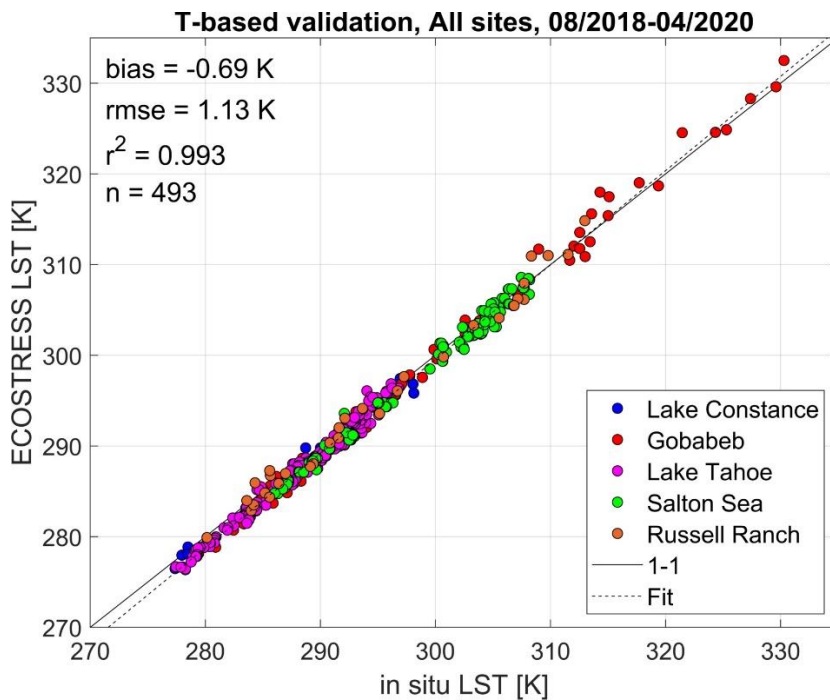


Figure 22. An example of the T-based validation results showing ECOSTRESS LST versus in situ LST measurements for all T-based sites at Lake Constance, Gobabeb, Lake Tahoe, Salton Sea and Russell ranch.

Acknowledgements

The research was carried out at the Jet Propulsion Laboratory, California Institute of Technology, under a contract with the National Aeronautics and Space Administration.

10 References

- Anderson, M.C., Norman, J.M., Mecikalski, J.R., Otkin, J.A., & Kustas, W.P. (2007). A climatological study of evapotranspiration and moisture stress across the continental United States based on thermal remote sensing: 2. Surface moisture climatology. *Journal of Geophysical Research-Atmospheres*, 112
- Augustine, J.A., DeLuisi, J.J., & Long, C.N. (2000). SURFRAD - A national surface radiation budget network for atmospheric research. *Bulletin of the American Meteorological Society*, 81, 2341-2357
- Baldrige, A.M., Hook, S.J., Grove, C.I., & Rivera, G. (2009). The ASTER Spectral Library Version 2.0. *Remote Sensing of Environment*, 114, 711-715
- Bannari, A., Omari, K., Teillet, R.A., & Fedosejevs, G. (2005). Potential of getis statistics to characterize the radiometric uniformity and stability of test sites used for the calibration of earth observation sensors. *Ieee Transactions on Geoscience and Remote Sensing*, 43, 2918-2926
- Barducci, A., & Pippi, I. (1996). Temperature and emissivity retrieval from remotely sensed images using the "grey body emissivity" method. *Ieee Transactions on Geoscience and Remote Sensing*, 34, 681-695
- Barton, I.J., Minnett, P.J., Maillet, K.A., Donlon, C.J., Hook, S.J., Jessup, A.T., & Nightingale, T.J. (2004). The Miami2001 infrared radiometer calibration and intercomparison. part II: Shipboard results. *Journal of Atmospheric and Oceanic Technology*, 21, 268-283
- Barton, I.J., Zavody, A.M., Obrien, D.M., Cutten, D.R., Saunders, R.W., & Llewellyn-Jones, D.T. (1989). Theoretical Algorithms for Satellite-Derived Sea-Surface Temperatures. *Journal of Geophysical Research-Atmospheres*, 94, 3365-3375
- Bauer, P., Moreau, E., Chevallier, F., & O'Keeffe, U. (2006). Multiple-scattering microwave radiative transfer for data assimilation applications. *Quarterly Journal of the Royal Meteorological Society*, 132, 1259-1281
- Becker, F., & Li, Z.L. (1990). Temperature-Independent Spectral Indexes in Thermal Infrared Bands. *Remote Sensing of Environment*, 32, 17-33
- Berk, A., Anderson, G.P., Acharya, P.K., Bernstein, L.S., Muratov, L., Lee, J., Fox, M., Adler-Golden, S.M., Chetwynd, J.H., Hoke, M.L., Lockwood, R.B., Gardner, J.A., Cooley, T.W., Borel, C.C., & Lewis, P.E. (2005). MODTRANTM 5, A Reformulated Atmospheric Band Model with Auxiliary Species and Practical Multiple Scattering Options: Update. In S.S. Sylvia, & P.E. Lewis (Eds.), in *Proc SPIE, Algorithms and Technologies for Multispectral, Hyperspectral, and Ultraspectral Imagery XI* (pp. 662-667). Bellingham, WA: Proceedings of SPIE
- Borbas, E., Seemann, S.W., Huang, H.L., Li, J., & Menzel, W.P. (2005). Global profile training database for satellite regression retrievals with estimates of skin temperature and emissivity. In, *Proc. of the Int. ATOVS Study Conference-XIV*
- Bosilovich, M.G., Chen, J.Y., Robertson, F.R., & Adler, R.F. (2008). Evaluation of global precipitation in reanalyses. *Journal of Applied Meteorology and Climatology*, 47, 2279-2299
- Brown, O., & Minnett, P. (1999). MODIS infrared sea surface temperature algorithm. *Algorithm Theoretical Basis Document Version 2*, Univ. of Miami, Miami, Fla.
- Chevallier, F. (2000). Sampled database of 60-level atmospheric profiles from the ECMWF analyses. In

- Coll, C., & Caselles, V. (1997). A split-window algorithm for land surface temperature from advanced very high resolution radiometer data: Validation and algorithm comparison. *Journal of Geophysical Research-Atmospheres*, *102*, 16697-16713
- Coll, C., Caselles, V., Galve, J.M., Valor, E., Niclos, R., Sanchez, J.M., & Rivas, R. (2005). Ground measurements for the validation of land surface temperatures derived from AATSR and MODIS data. *Remote Sensing of Environment*, *97*, 288-300
- Coll, C., Wan, Z.M., & Galve, J.M. (2009a). Temperature-based and radiance-based validations of the V5 MODIS land surface temperature product. *Journal of Geophysical Research-Atmospheres*, *114*, D20102, doi:20110.21029/22009JD012038
- Coll, C., Wan, Z.M., & Galve, J.M. (2009b). Temperature-based and radiance-based validations of the V5 MODIS land surface temperature product. *Journal of Geophysical Research-Atmospheres*, *114*, -
- Cook, M. (2014). Atmospheric Compensation for a Landsat Land Surface Temperature Product. In, *Chester F. Carlson Center for Imaging Science*. Rochester: Rochester Institute of Technology
- Cosnefroy, H.N., Leroy, M., & Briottet, X. (1996). Selection and characterization of Saharan and Arabian desert sites for the calibration of optical satellite sensors. *Remote Sensing of Environment*, *58*, 101-114
- Coudert, B., Otle, C., Boudevillain, B., Demarty, J., & Guillevic, P. (2006). Contribution of thermal infrared remote sensing data in multiobjective calibration of a dual-source SVAT model. *Journal of Hydrometeorology*, *7*, 404-420
- de Vries, C., Danaher, T., Denham, R., Scarth, P., & Phinn, S. (2007). An operational radiometric calibration procedure for the Landsat sensors based on pseudo-invariant target sites. *Remote Sensing of Environment*, *107*, 414-429
- Deschamps, P.Y., & Phulpin, T. (1980). Atmospheric Correction of Infrared Measurements of Sea-Surface Temperature Using Channels at 3.7, 11 and 12 μ -m. *Boundary-Layer Meteorology*, *18*, 131-143
- Eyre, J.R., & Woolf, H.M. (1988). Transmittance of Atmospheric Gases in the Microwave Region - a Fast Model. *Applied Optics*, *27*, 3244-3249
- French, A.N., Jacob, F., Anderson, M.C., Kustas, W.P., Timmermans, W., Gieske, A., Su, Z., Su, H., McCabe, M.F., Li, F., Prueger, J., & Brunsell, N. (2005). Surface energy fluxes with the Advanced Spaceborne Thermal Emission and Reflection radiometer (ASTER) at the Iowa 2002 SMACEX site (USA) (vol 99, pg 55, 2005). *Remote Sensing of Environment*, *99*, 471-471
- French, A.N., Schmugge, T.J., Ritchie, J.C., Hsu, A., Jacob, F., & Ogawa, K. (2008). Detecting land cover change at the Jornada Experimental Range, New Mexico with ASTER emissivities. *Remote Sensing of Environment*, *112*, 1730-1748
- Galve, J.A., Coll, C., Caselles, V., & Valor, E. (2008). An atmospheric radiosounding database for generating land surface temperature algorithms. *IEEE Transactions on Geoscience and Remote Sensing*, *46*, 1547-1557
- Gillespie, A., Rokugawa, S., Hook, S., Matsunaga, T., & Kahle, A.B. (1999). Temperature/Emissivity Separation Algorithm Theoretical Basis Document, Version 2.4, ASTER TES ATBD, NASA Contract NAS5-31372, 31322 March, 31999
- Gillespie, A., Rokugawa, S., Matsunaga, T., Cothorn, J.S., Hook, S., & Kahle, A.B. (1998). A temperature and emissivity separation algorithm for Advanced Spaceborne Thermal Emission and Reflection Radiometer (ASTER) images. *Ieee Transactions on Geoscience and Remote Sensing*, *36*, 1113-1126

- Gottsche, F.M., & Hulley, G.C. (2012a). Validation of six satellite-retrieved land surface emissivity products over two land cover types in a hyper-arid region. *Remote Sensing of Environment*, 124, 149-158
- Gottsche, F.M., & Hulley, G.C. (2012b). Validation of six satellite-retrieved land surface emissivity products over two land cover types in a hyper-arid region. *Remote Sensing of Environment*, 124, 149-158
- Guillevic, P., Privette, J.L., Coudert, B., Palecki, M.A., Demarty, J., Otle, C., & Augustine, J.A. (2012). Land Surface Temperature product validation using NOAA's surface climate observation networks—Scaling methodology for the Visible Infrared Imager Radiometer Suite (VIIRS). *Remote Sensing of Environment*, 124, 282-298
- Gustafson, W.T., Gillespie, A.R., & Yamada, G.J. (2006). Revisions to the ASTER temperature/emissivity separation algorithm. In, *2nd International Symposium on Recent Advances in Quantitative Remote Sensing*. Torrent (Valencia), Spain
- Hook, S.J., Chander, G., Barsi, J.A., Alley, R.E., Abtahi, A., Palluconi, F.D., Markham, B.L., Richards, R.C., Schladow, S.G., & Helder, D.L. (2004). In-flight validation and recovery of water surface temperature with Landsat-5 thermal infrared data using an automated high-altitude lake validation site at Lake Tahoe. *Ieee Transactions on Geoscience and Remote Sensing*, 42, 2767-2776
- Hook, S.J., Dmochowski, J.E., Howard, K.A., Rowan, L.C., Karlstrom, K.E., & Stock, J.M. (2005). Mapping variations in weight percent silica measured from multispectral thermal infrared imagery - Examples from the Hiller Mountains, Nevada, USA and Tres Virgenes-La Reforma, Baja California Sur, Mexico. *Remote Sensing of Environment*, 95, 273-289
- Hook, S.J., Gabell, A.R., Green, A.A., & Kealy, P.S. (1992). A Comparison of Techniques for Extracting Emissivity Information from Thermal Infrared Data for Geologic Studies. *Remote Sensing of Environment*, 42, 123-135
- Hook, S.J., Prata, F.J., Alley, R.E., Abtahi, A., Richards, R.C., Schladow, S.G., & Palmansson, S.O. (2003). Retrieval of lake bulk and skin temperatures using Along-Track Scanning Radiometer (ATSR-2) data: A case study using Lake Tahoe, California. *Journal of Atmospheric and Oceanic Technology*, 20, 534-548
- Hook, S.J., Vaughan, R.G., Tonooka, H., & Schladow, S.G. (2007). Absolute radiometric in-flight validation of mid infrared and thermal infrared data from ASTER and MODIS on the terra spacecraft using the Lake Tahoe, CA/NV, USA, automated validation site. *Ieee Transactions on Geoscience and Remote Sensing*, 45, 1798-1807
- Hulley, G., Hook, S., & Hughes, C. (2012a). MODIS MOD21 Land Surface Temperature and Emissivity Algorithm Theoretical Basis Document. In: Jet Propulsion Laboratory, California Institute of Technology, JPL Publication 12-17, August, 2012
- Hulley, G.C., Gottsche, F.M., Rivera, G., Hook, S.J., Freepartner, R.J., Martin, M.A., Cawse-Nicholson, K., & Johnson, W.R. (2022). Validation and Quality Assessment of the ECOSTRESS Level-2 Land Surface Temperature and Emissivity Product. *Ieee Transactions on Geoscience and Remote Sensing*, 60
- Hulley, G.C., & Hook, S.J. (2009a). Intercomparison of Versions 4, 4.1 and 5 of the MODIS Land Surface Temperature and Emissivity Products and Validation with Laboratory Measurements of Sand Samples from the Namib Desert, Namibia. *Remote Sensing of Environment*, 113, 1313-1318
- Hulley, G.C., & Hook, S.J. (2009b). The North American ASTER Land Surface Emissivity Database (NAALSED) Version 2.0. *Remote Sensing of Environment*, 113, 1967-1975

- Hulley, G.C., & Hook, S.J. (2011). Generating Consistent Land Surface Temperature and Emissivity Products Between ASTER and MODIS Data for Earth Science Research. *Ieee Transactions on Geoscience and Remote Sensing*, 49, 1304-1315
- Hulley, G.C., & Hook, S.J. (2012). A radiance-based method for estimating uncertainties in the Atmospheric Infrared Sounder (AIRS) land surface temperature product. *Journal of Geophysical Research-Atmospheres*, 117
- Hulley, G.C., Hook, S.J., & Baldrige, A.M. (2008). ASTER land surface emissivity database of California and Nevada. *Geophysical Research Letters*, 35, L13401, doi: 10.1029/2008gl034507
- Hulley, G.C., Hook, S.J., & Baldrige, A.M. (2009a). Validation of the North American ASTER Land Surface Emissivity Database (NAALSED) Version 2.0 using Pseudo-Invariant Sand Dune Sites. *Remote Sensing of Environment*, 113, 2224-2233
- Hulley, G.C., Hook, S.J., Manning, E., Lee, S.Y., & Fetzer, E.J. (2009b). Validation of the Atmospheric Infrared Sounder (AIRS) Version 5 (v5) Land Surface Emissivity Product over the Namib and Kalahari Deserts. *Journal of Geophysical Research Atmospheres*, 114, D19104
- Hulley, G.C., Hughes, T., & Hook, S.J. (2012b). Quantifying Uncertainties in Land Surface Temperature (LST) and Emissivity Retrievals from ASTER and MODIS Thermal Infrared Data. *Journal of Geophysical Research Atmospheres*, in press.
- Jimenez-Munoz, J.C., & Sobrino, J.A. (2010). A Single-Channel Algorithm for Land-Surface Temperature Retrieval From ASTER Data. *Ieee Geoscience and Remote Sensing Letters*, 7, 176-179
- Jin, M.L., & Dickinson, R.E. (2010). Land surface skin temperature climatology: benefitting from the strengths of satellite observations. *Environmental Research Letters*, 5, -
- Justice, C., & Townshend, J. (2002). Special issue on the moderate resolution imaging spectroradiometer (MODIS): a new generation of land surface monitoring. *Remote Sensing of Environment*, 83, 1-2
- Kalnay, E., Kanamitsu, M., & Baker, W.E. (1990). Global Numerical Weather Prediction at the National-Meteorological-Center. *Bulletin of the American Meteorological Society*, 71, 1410-1428
- Kealy, M.J., Montgomery, M., & Dovidio, J.F. (1990). Reliability and Predictive-Validity of Contingent Values - Does the Nature of the Good Matter. *Journal of Environmental Economics and Management*, 19, 244-263
- Kealy, P.S., & Hook, S. (1993). Separating temperature & emissivity in thermal infrared multispectral scanner data: Implication for recovering land surface temperatures. *Ieee Transactions on Geoscience and Remote Sensing*, 31, 1155-1164
- Kneizys, F.X., Abreu, L.W., Anderson, G.P., Chetwynd, J.H., Shettle, E.P., Berk, A., Bernstein, L.S., Robertson, D.C., Acharya, P.K., Rothman, L.A., Selby, J.E.A., Gallery, W.O., & Clough, S.A. (1996). The MODTRAN 2/3 Report & LOWTRAN 7 Model, F19628-91-C-0132. In, *Phillips Lab. Hanscom AFB, MA*
- Li, F.Q., Jackson, T.J., Kustas, W.P., Schmugge, T.J., French, A.N., Cosh, M.H., & Bindlish, R. (2004). Deriving land surface temperature from Landsat 5 and 7 during SMEX02/SMACEX. *Remote Sensing of Environment*, 92, 521-534
- Lucchesi, R. (2017). File Specification for GEOS-5 FP. GMAO Office Note No. 4 (Version 1.1), 61 pp, available from http://gmao.gsfc.nasa.gov/pubs/office_notes. In
- Lyon, R. (1965). Analysis of ROcks by Spectral INfrared Emission (8 to 25 microns). *Economic Geology and the Bulletin of the Society of Economic Geologists*, 60, 715-736

- Masuda, K., Takashima, T., & Takayama, Y. (1988). Emissivity of Pure and Sea Waters for the Model Sea-Surface in the Infrared Window Regions. *Remote Sensing of Environment*, 24, 313-329
- Matricardi, M. (2008). The generation of RTTOV regression coefficients for IASI and AIRS using a new profile training set and a new line-by-line database. In: ECMWF Research Dept. Tech. Memo.
- Matricardi, M. (2009). Technical Note: An assessment of the accuracy of the RTTOV fast radiative transfer model using IASI data. *Atmospheric Chemistry and Physics*, 9, 6899-6913
- Matricardi, M., Chevallier, F., Kelly, G., & Thepaut, J.N. (2004). An improved general fast radiative transfer model for the assimilation of radiance observations. *Quarterly Journal of the Royal Meteorological Society*, 130, 153-173
- Matricardi, M., Chevallier, F., & Tjemkes, S.A. (2001). An improved general fast radiative transfer model for the assimilation of radiance observations. In: European Centre for Medium-Range Weather Forecasts
- Matricardi, M., & Saunders, R. (1999). Fast radiative transfer model for simulation of infrared atmospheric sounding interferometer radiances. *Applied Optics*, 38, 5679-5691
- Matsunaga, T. (1994). A temperature-emissivity separation method using an empirical relationship between the mean, the maximum, & the minimum of the thermal infrared emissivity spectrum, in Japanese with English abstract. *Journal Remote Sensing Society Japan*, 14, 230-241
- Meerdink, S.K., Hook, S.J., Roberts, D.A., & Abbott, E.A. (2019). The ECOSTRESS spectral library version 1.0. *Remote Sensing of Environment*, 230
- Mesinger, F., DiMego, G., Kalnay, E., Mitchell, K., Shafran, P.C., Ebisuzaki, W., Jovic, D., Woollen, J., Rogers, E., Berbery, E.H., Ek, M.B., Fan, Y., Grumbine, R., Higgins, W., Li, H., Lin, Y., Manikin, G., Parrish, D., & Shi, W. (2006). North American regional reanalysis. *Bulletin of the American Meteorological Society*, 87, 343-+
- Mira, M., Valor, E., Boluda, R., Caselles, V., & Coll, C. (2007). Influence of soil water content on the thermal infrared emissivity of bare soils: Implication for land surface temperature determination. *Journal of Geophysical Research-Earth Surface*, 112, F04003
- Mushkin, A., & Gillespie, A.R. (2005). Estimating sub-pixel surface roughness using remotely sensed stereoscopic data. *Remote Sensing of Environment*, 99, 75-83
- Norman, J.M., & Becker, F. (1995). Terminology in Thermal Infrared Remote-Sensing of Natural Surfaces. *Agricultural and Forest Meteorology*, 77, 153-166
- Ogawa, K., Schmugge, T., & Rokugawa, S. (2006). Observations of the dependence of the thermal infrared emissivity on soil moisture. *Geophysical Research Abstracts*, 8, 04996
- Palluconi, F., Hoover, G., Alley, R.E., Nilsen, M.J., & Thompson, T. (1999). An atmospheric correction method for ASTER thermal radiometry over land, ASTER algorithm theoretical basis document (ATBD), Revision 3, Jet Propulsion Laboratory, Pasadena, CA, 1999
- Prata, A.J. (1994). Land-Surface Temperatures Derived from the Advanced Very High-Resolution Radiometer and the Along-Track Scanning Radiometer .2. Experimental Results and Validation of Avhrr Algorithms. *Journal of Geophysical Research-Atmospheres*, 99, 13025-13058
- Price, J.C. (1984). Land surface temperature measurements from the split window channels of the NOAA 7 Advanced Very High Resolution Radiometer. *Journal of Geophysical Research*, 89, 7231-7237

- Saunders, R., Matricardi, M., & Brunel, P. (1999). An improved fast radiative transfer model for assimilation of satellite radiance observations. *Quarterly Journal of the Royal Meteorological Society*, *125*, 1407-1425
- Seemann, S.W., Borbas, E., Li, J., Menzel, P., & Gumley, L.E. (2006). MODIS Atmospheric Profile Retrieval Algorithm Theoretical Basis Document, Cooperative Institute for Meteorological Satellite Studies, University of Wisconsin-Madison, Madison, WI, Version 6, October 25, 2006
- Snyder, W.C., Wan, Z., Zhang, Y., & Feng, Y.Z. (1998). Classification-based emissivity for land surface temperature measurement from space. *International Journal of Remote Sensing*, *19*, 2753-2774
- Strow, L.L., Hannon, S.E., Machado, S.D.S., Motteler, H.E., & Tobin, D.C. (2006). Validation of the Atmospheric Infrared Sounder radiative transfer algorithm. *Journal of Geophysical Research-Atmospheres*, *111*
- Susskind, J., Barnett, C.D., & Blaisdell, J.M. (2003). Retrieval of atmospheric and surface parameters from AIRS/AMSU/HSB data in the presence of clouds. *Ieee Transactions on Geoscience and Remote Sensing*, *41*, 390-409
- Teillet, P.M., Fedosejevs, G., Gautier, R.P., & Schowengerdt, R.A. (1998). Uniformity characterization of land test sites used for radiometric calibration of earth observation sensors. In, *Proc. 20th Can. Symp. Remote Sensing* (pp. 1-4). Calgary, AB, Canada
- Tonooka, H. (2001). An atmospheric correction algorithm for thermal infrared multispectral data over land - A water-vapor scaling method. *Ieee Transactions on Geoscience and Remote Sensing*, *39*, 682-692
- Tonooka, H. (2005). Accurate atmospheric correction of ASTER thermal infrared imagery using the WVS method. *Ieee Transactions on Geoscience and Remote Sensing*, *43*, 2778-2792
- Tonooka, H., Palluconi, F.D., Hook, S.J., & Matsunaga, T. (2005). Vicarious calibration of ASTER thermal infrared bands. *Ieee Transactions on Geoscience and Remote Sensing*, *43*, 2733-2746
- Vaughan, R.G., Hook, S.J., Calvin, W.M., & Taranik, J.V. (2005). Surface mineral mapping at Steamboat Springs, Nevada, USA, with multi-wavelength thermal infrared images. *Remote Sensing of Environment*, *99*, 140-158
- Wan, Z., & Li, Z.L. (2008). Radiance-based validation of the V5 MODIS land-surface temperature product. *International Journal of Remote Sensing*, *29*, 5373-5395
- Wan, Z.M. (2008). New refinements and validation of the MODIS Land-Surface Temperature/Emissivity products. *Remote Sensing of Environment*, *112*, 59-74
- Wan, Z.M., & Dozier, J. (1996). A generalized split-window algorithm for retrieving land-surface temperature from space. *Ieee Transactions on Geoscience and Remote Sensing*, *34*, 892-905
- Wan, Z.M., & Li, Z.L. (1997). A physics-based algorithm for retrieving land-surface emissivity and temperature from EOS/MODIS data. *Ieee Transactions on Geoscience and Remote Sensing*, *35*, 980-996
- Wang, K.C., & Liang, S.L. (2009). Evaluation of ASTER and MODIS land surface temperature and emissivity products using long-term surface longwave radiation observations at SURFRAD sites. *Remote Sensing of Environment*, *113*, 1556-1565
- Watson, K. (1992). Spectral Ratio Method for Measuring Emissivity. *Remote Sensing of Environment*, *42*, 113-116
- Watson, K., Kruse, F.A., & Hummermilller, S. (1990). Thermal Infrared Exploration in the Carlin Trend, Northern Nevada. *Geophysics*, *55*, 70-79

Yu, Y., Privette, J.L., & Pinheiro, A.C. (2008). Evaluation of split-window land surface temperature algorithms for generating climate data records. *Ieee Transactions on Geoscience and Remote Sensing*, 46, 179-192